

## AN EQUATION OF STATE FOR SILICATE MELTS. IV. CALIBRATION OF A MULTICOMPONENT MIXING MODEL TO 40 GPa

MARK S. GHIORSO

Department of Geophysical Sciences, The University of Chicago,  
5723 S. Ellis Avenue, Chicago, Illinois 60637; ghiorso@geosci.uchicago.edu

**ABSTRACT.** Mixing relations for the “high-pressure” parameters of the equation of state of Ghiorso (2004a) are developed and compositional coefficients are optimized to permit calculation of melt density in portions of the system  $\text{SiO}_2\text{-TiO}_2\text{-Al}_2\text{O}_3\text{-FeO-MgO-CaO-Na}_2\text{O-K}_2\text{O}$  to pressures in excess of 40 GPa and temperatures up to 2500°C. Four data sets are analyzed and fitted to yield an internally consistent model: (1) density estimates made from measurements of the sinking/floating of reference mineral markers in silicate liquids at known temperatures and pressures, (2) density estimates obtained from shock compression studies on molten liquids, (3) liquid densities inferred from the temperature and pressure dependence of the slopes of mineral fusion curves, and (4) estimates of densities of molten silicate liquids obtained by molecular dynamics simulations. Calibration compositions include chemically complex liquids (komatiite, peridotite and MORB bulk compositions) as well as simple liquids with mineral-like stoichiometry. The model recovers density with an average error of  $\sim 2$  percent. The model is limited by *not* including the effects of volatiles or oxidized iron at elevated pressure.

### INTRODUCTION

This is the fourth contribution in a series of papers reporting on the formulation and calibration of a new equation of state (EOS) for multicomponent silicate liquids. A rationale for the EOS is developed in the first paper of the series (Ghiorso, 2004a, hereafter Part I) while the second paper (Ghiorso and Kress, 2004, hereafter Part II) deals with calibration of model parameters in the system  $\text{SiO}_2\text{-TiO}_2\text{-Al}_2\text{O}_3\text{-Fe}_2\text{O}_3\text{-FeO-MgO-NiO-CoO-CaO-Na}_2\text{O-K}_2\text{O}$  at the reference pressure ( $10^5$  Pa). The third paper in the series (Ghiorso 2004b, hereafter Part III) demonstrates the applicability of the EOS for modeling (1) experimental data on pressure ( $P$ )- temperature ( $T$ ) paths of fusion curves for a variety of silicate minerals, (2) estimates of melt density derived from molecular dynamics simulation, and (3) the Hugoniot obtained from shock-compression experiments on both compositionally simple and complex silicate liquids. In this paper the fusion curve, molecular dynamics and shock-compression data are reexamined along with density constraints obtained from “sink-float” experiments in piston-cylinder and multianvil apparatus. Selected observations from the four data sets are combined to derive EOS parameter values that permit estimation of the densities of multicomponent silicate melts in portions of the system  $\text{SiO}_2\text{-TiO}_2\text{-Al}_2\text{O}_3\text{-FeO-MgO-CaO-Na}_2\text{O-K}_2\text{O}$  to pressures on the order of 40 GPa and temperatures up to 2500°C.

The work reported here has application beyond the estimation of density contrast between partial melts and accompanying solids in silicate planetary interiors. All thermodynamic properties of silicate melts at elevated pressures are derived from an EOS for the liquid. This work will allow thermodynamic models for magmatic-composition liquids, which are calibrated from experimental phase equilibrium data obtained at low to moderate pressures (for example, Ghiorso and Sack, 1995; Ghiorso and others, 2002), to be extrapolated to pressures that correspond to depths in the Earth’s interior at approximately the base of the mantle transition zone. Application of the EOS to the calculation of magmatic phase relations at elevated pressure will be the subject of a future contribution.

The outline of this paper is to first review the functional form of the EOS proposed in Part I and then to summarize the mixing relations established in Part II for reference pressure model parameters. Algorithms for high-pressure parameter mixing relations are then specified. Next, data sets relevant to the calibration of these high-pressure parameter mixing-models are examined and a method is described to combine various kinds of data (for example, fusion curve constraints, shock-compression Hugoniot, sink-float density brackets, molecular dynamics density estimates) in a coherent fashion in order to formulate an optimization problem for unbiased parameter regression. Lastly, the data sets are fitted by weighted non-linear least squares regression and data recovery is examined.

#### MIXING RELATIONS

The liquid EOS developed in Part I is of the form

$$V = \frac{V_0 + (V_1 + V_0 a)(P - P_r) + \left(\frac{V_2}{2} + V_1 a + V_0 b\right)(P - P_r)^2}{1 + a(P - P_r) + b(P - P_r)^2} \quad (1)$$

where the “ $a$ ” and “ $b$ ” parameters in the denominator of equation (1) may be expressed alternately as

$$a = \frac{V_2 V_3 - \frac{1}{2} V_1 V_4}{2 V_1 V_3 - 3 V_2^2} \quad (2)$$

and

$$b = \frac{\frac{1}{4} V_2 V_4 - \frac{1}{3} V_3^2}{2 V_1 V_3 - 3 V_2^2} \quad (3)$$

In equations (1) - (3),  $V$  is the volume,  $P$  the pressure, and  $V_0, V_1, V_2, V_3, V_4$  are model parameters corresponding to pressure-derivatives of the volume, that is  $V_i = \frac{\partial^i V}{\partial P^i}$ . At the reference pressure ( $P_r$ ) of  $10^5$  Pa, equation (1) reduces to  $V = V_0$  and the pressure derivative of  $V$  may be shown to be (Part I)  $\frac{\partial V}{\partial P} = V_1$ .

In Part II the parameter  $V_0$  is modeled as

$$V_0 = V_{0,T_r} e^{\alpha(T - T_r)} \quad (4)$$

where the thermal expansion ( $\alpha$ ) is expressed as

$$\alpha = \frac{1}{V_{0,T_r}} \left. \frac{\partial V_{T_r}}{\partial T} \right|_{T_r} \quad (5)$$

Both the reference temperature ( $T_r = 1400^\circ\text{C}$ ) volume ( $V_{0,T_r}$ ) and the temperature derivative of the volume at the reference temperature ( $\left. \frac{\partial V_{T_r}}{\partial T} \right|_{T_r}$ ) are found to be linear

functions of the number of moles of oxides ( $n_i$ ) in a multicomponent liquid<sup>1</sup>, for example

$$V_{0,T_r} = \sum_i n_i \bar{v}_{i,T_r} \quad (6)$$

and

$$\left. \frac{\partial V_{T,P_r}}{\partial T} \right|_{T_r} = \sum_i n_i \frac{\partial \bar{v}_i}{\partial T} \quad (7)$$

Equations (6) and (7) represent linear mixing relations and the mixing parameters ( $\bar{v}_{i,T_r}$  and  $\frac{\partial \bar{v}_i}{\partial T}$ ) may be interpreted as *partial molar* quantities.

The pressure derivative of the volume at the reference pressure ( $V_1$ ) is a derived quantity obtained from measurements of the reference-pressure sound speed ( $c$ )

$$V_1 = -V_{0,T_r}^2 \left( \frac{1}{Mc^2} + \frac{T\alpha^2}{C_p} \right) [e^{\alpha(T-T_r)}]^2 \quad (8)$$

(Part II), where  $M$  is the gram-formula weight and  $C_p$  is the heat capacity of the liquid, both of which are modeled as linear functions of mole numbers

$$C_p = \sum_i n_i \bar{c}_{p,i} \quad (9)$$

$$M = \sum_i n_i MW_i \quad (10)$$

In equation (10), the  $MW_i$  are molecular weights of the oxide constituents. The quantity  $c$  is an intensive thermodynamic variable that is parameterized in Part II by

$$c = \sum_i X_i \left[ \bar{c}_i \Big|_{1673K} + \frac{\partial \bar{c}_i}{\partial T} (T - 1673) \right] + X_{\text{Na}_2\text{O}} X_{\text{Al}_2\text{O}_3} \bar{c}_{\text{Na-Al}} + X_{\text{Na}_2\text{O}} X_{\text{TiO}_2} \bar{c}_{\text{Na-Ti}} \\ + X_{\text{K}_2\text{O}} X_{\text{TiO}_2} \bar{c}_{\text{K-Ti}} \quad (11)$$

where the  $X_i$  are oxide mole fractions. Cumulatively, the relations (8), (9), (10) and (11) induce a non-linear compositional and temperature dependence to  $V_1$ . Equations (6), (7), (9), (10) and (11) embody the mixing relations for the reference pressure EOS parameters.

The mixing relations for EOS parameters operative at pressures above  $P_r$ , namely  $V_2$ ,  $V_3$ , and  $V_4$ , remain to be defined. Of foremost concern in the selection of these relations is simplicity of formulation. Data available for the calibration of high-pressure

<sup>1</sup>For liquids that contain significant concentrations of  $\text{TiO}_2$  and an alkali-metal oxide, the partial molar volume of  $\text{TiO}_2$  and its temperature derivative should be written (eqs 24 and 25 of Part II):

$$\bar{v}_{\text{TiO}_2,T_r} = \bar{v}_{\text{ref-TiO}_2,T_r} + X_{\text{Na}_2\text{O}} \bar{v}_{\text{Na}_2\text{O-TiO}_2,T_r} + X_{\text{K}_2\text{O}} \bar{v}_{\text{K}_2\text{O-TiO}_2,T_r} \\ \frac{\partial \bar{v}_{\text{TiO}_2,T_r}}{\partial T} = \frac{\partial \bar{v}_{\text{ref-TiO}_2,T_r}}{\partial T} + X_{\text{Na}_2\text{O}} \frac{\partial \bar{v}_{\text{Na}_2\text{O-TiO}_2,T_r}}{\partial T} + X_{\text{K}_2\text{O}} \frac{\partial \bar{v}_{\text{K}_2\text{O-TiO}_2,T_r}}{\partial T}$$

where the  $X$  are mole fractions calculated on an oxide basis. In naturally occurring silicate liquids, the extra quadratic compositional terms are not required.

EOS parameters are scarce and subject to much greater uncertainty than low-pressure density and sound speed measurements. Compositional coverage is not as broad and temperature tends to be correlated with pressure in the majority of the available data sets. Mixing relations are sought that can accommodate these data at or near the level of precision of measurement while at the same time allow stable extrapolation to compositions not studied. The latter requirement motivates a minimal number of mixing terms and a simple functional form for these relations. In devising the liquid EOS (Part I) one simplifying assumption was anticipated and built into the formulation. This assumption involves the temperature dependence of the higher-order pressure parameters. It is assumed that the terms “ $a$ ”, “ $b$ ” and  $V_2$  in equation (1) are independent of  $T$ , which demands that the parameters  $V_3$ , and  $V_4$  inherit their temperature dependence from  $V_1$  as follows (Part I)

$$\frac{\partial V_3}{\partial T} = -6b \frac{\partial V_1}{\partial T} \quad (12)$$

$$\frac{\partial V_4}{\partial T} = 24ab \frac{\partial V_1}{\partial T} \quad (13)$$

To this simplifying assumption regarding temperature-dependence of the higher-order pressure terms, linear mixing of  $V_2$  at all  $T$  and  $P$  is postulated

$$V_2 = \sum_i n_i \bar{v}_{2,i} \quad (14)$$

along with linear mixing of  $V_3$  and  $V_4$  at the reference-temperature.

$$V_3 = \sum_i n_i \bar{v}_{3,i} \quad (15)$$

$$V_4 = \sum_i n_i \bar{v}_{4,i} \quad (16)$$

The mole numbers ( $n_i$ ) refer as above to oxide components. Equations (14), (15) and (16) embody the mixing relations for the high-pressure EOS parameters. The parameters  $\bar{v}_{2,i}$ ,  $\bar{v}_{3,i}$ , and  $\bar{v}_{4,i}$  require calibration from experimental data sets.

Before turning to a discussion of data sources and calibration procedures, it is worth noting that the adoption of linear mixing relations for the higher-order pressure parameters *does not* imply linear mixing of  $V$  at elevated pressure. Nonlinearity at  $P$  is an unavoidable consequence of using any EOS with a functional form more complex than a simple polynomial expansion in  $P$ .

#### DATA SETS FOR CALIBRATION

Four types of data are available for calibration of the higher-order mixing parameters of the EOS. Three of these data sets are the subject of analysis in Part III. They include (1) thermodynamic constraints on the pressure-integral of the volume as inferred from mineral fusion curves, (2) estimates of melt density from molecular dynamics simulations, and (3) density-pressure relations derived from shock-compression Hugoniot. The molecular dynamics simulations also facilitate the unambiguous correlation of melt density with melt structure. This information is essential for developing model EOS parameterizations that account solely for *vibrational* contri-

butions to the volume of the liquid (Part I, Part III).<sup>2</sup> Fusion curve, molecular dynamics and shock-compression data are analyzed in Part III as a series of  $T$ - $P$  constraints on density from which  $V_2$ ,  $V_3$ , and  $V_4$  parameters are estimated for a given bulk composition. Internal consistency of EOS parameter estimates *across the whole of composition-space* is not a concern of the previous analysis but it is central to the present calibration effort. These data are reexamined here with that objective in mind.

The data sets explored in Part III largely provide constraints on compositionally simple liquids of mineral-like stoichiometry. The fourth data resource considered in this paper generate density constraints on liquids that more closely approximate compositions found in nature. These data are bounds on liquid density obtained from experimental determinations of the sinking or floating of solid materials in melts at specified  $T$  and  $P$ . Experiments of this kind are referred to as *sink-float* experiments. Typically, sink-float experiments are performed in piston cylinder or multi-anvil apparatus with solid density index materials that are inert or are in equilibrium with the liquid, such as olivine, garnet or diamond.

Sink-float density estimates have been culled from the literature and data sources and experimental conditions are summarized in table 1. The experiments of Ohtani and others (1995, 1998), Suzuki and Ohtani (2003) and Suzuki and others (1995, 1998), utilizing both diamond and olivine as index markers, were performed on analogue peridotite and Fe-enriched peridotite compositions in the system CaO-MgO- $\text{Al}_2\text{O}_3$ - $\text{SiO}_2$ -FeO (CMASF). Magnesium numbers ( $\text{Mg\#} = \frac{\text{wt\%MgO}}{\text{wt\%MgO} + \text{wt\%FeO}}$ ) of experimental liquids range from 1.9 to 4.7. Ohtani and Maeda (2001) describe sink-float density experiments on a MORB bulk composition (in CMASF +  $\text{Na}_2\text{O}$ ) and a picritic melt (in CMASF +  $\text{MnO}$  +  $\text{TiO}_2$  +  $\text{Cr}_2\text{O}_3$ ). The work of Agee and Walker (1988, 1993) reports density brackets obtained from sinking and floating of olivine in CMASF analogue liquids of komatiite- and peridotite-like bulk composition. These authors selectively added excess iron in the form of  $\text{Fe}_2\text{SiO}_4$  to the experimental charges in order to achieve Mg#s ranging from 0.3 to 7.9. Sink-float measurements on a high-Ti lunar mare glass composition are reported by Circone and Agee (1996) and on a low-Ti mare glass composition by Smith and Agee (1997). Both sets of experiments were carried out in Mo-capsules, which resulted in contamination of the liquid; analyzed  $\text{MoO}_3$  is as high as 4.2 weight percent in quenched glasses from the highest temperature runs of Circone and Agee (1996). Additional sink-float density estimates on simple composition melts are reported by Agee (1992a, 1992b,  $\text{Fe}_2\text{SiO}_4$  liquid) and Knoche and Luth (1996, two compositions in the binary system  $\text{Na}_2\text{O}$ - $\text{SiO}_2$ , with 20.2 and 35.3 mole %  $\text{Na}_2\text{O}$ ). The first set of experiments are utilized in Part III in conjunction with other constraints on the density of  $\text{Fe}_2\text{SiO}_4$  liquid. Agee's (1992b) experiments are especially noteworthy in that they place tight bounds on the thermal expansion of  $\text{Fe}_2\text{SiO}_4$  liquid at pressure.

In addition to being the primary source of information on the densities of compositionally mixed silicate liquids at high pressure, the sink-float experiments are a fundamental source of information on iron-bearing systems. In the sink-float work on ultramafic liquid compositions, much of the focus is on the variation of melt density with iron-magnesium ratio (Mg#). These results compliment the fusion curve and shock compression data on molten  $\text{Fe}_2\text{SiO}_4$  and the shock compression data on komatiite (Miller and others, 1991) and MORB liquids (Rowan, ms, 1993). Taken together, the data sets explore a wide range of Fe-contents, and should provide strict

<sup>2</sup>Configurational contributions to the volume arise from structural changes in the liquid that accompany changes in  $T$ ,  $P$  or composition. Vibrational contributions refer to volumetric changes in an iso-structural standard state.

TABLE 1  
Sources and statistical analysis of data sets

Source	Number of data points	% std error in $\rho$ (data uncertainty)	% Systematic error in $\rho$ (model estimate) <sup>a</sup>	% std error in $\rho$ (model estimate)
<b>Sink-float Experiments</b>				
Agee (1992a, 1992b) <sup>b</sup>	23	Est. 1%	0.38	1.92
Agee and Walker (1988, 1993) <sup>f</sup>	35	Est. 1%	0.85	1.37
Circone and Agee (1996) <sup>d</sup>	17	Est. 1%	-0.09	0.44
Knoche and Luth (1996) <sup>c</sup>	9		-0.11	1.15
Ohtani and Maeda (2001) <sup>f</sup>	13	Est. 1%	0.19	0.51
Ohtani and others (1995) <sup>g</sup>	7	Est. 1%	0.17	0.37
Ohtani and others (1998) <sup>h</sup>	4	Est. 1%	0.40	1.42
Smith and Agee (1997) <sup>i</sup>	4	Est. 1%	-0.07	0.14
Suzuki and Ohtani (2003) <sup>j</sup>	18	Est. 1%	-0.11	1.15
Suzuki and others (1995, 1998) <sup>k</sup>	20	Est. 1%	-0.08	0.83
<b>Shock Compression Experiments</b>				
Chen and others (2002)	7	2.90% <sup>l</sup>	-0.35	2.72
Miller and others (1991)	12	0.74%	-0.64	1.32
Rigden and others (1984, 1989)	8	0.97%	-0.10	4.33
Rigden and others (1989, CaMgSi <sub>2</sub> O <sub>6</sub> )	5	1.03%	1.27	2.10
Rigden and others (1989, CaAl <sub>2</sub> Si <sub>2</sub> O <sub>8</sub> )	6	0.96%	(5.81) <sup>m</sup>	(8.27)
Rowan (1993)	12	3.14%	-6.32	7.00
<b>Fusion curves (sources: Part III)</b>				
Albite -> NaAlSi <sub>3</sub> O <sub>8</sub>	42	Est. 1%	(0.01)	(1.08)
Anorthite -> CaAl <sub>2</sub> Si <sub>2</sub> O <sub>8</sub>	6	Est. 1%	-0.15	0.36
Diopside -> CaMgSi <sub>2</sub> O <sub>6</sub>	64	Est. 1%	-0.67	1.14
Enstatite -> Mg <sub>2</sub> Si <sub>2</sub> O <sub>6</sub>	33	Est. 1%	(1.59)	(2.16)
Fayalite -> Fe <sub>2</sub> SiO <sub>4</sub>	85	Est. 1%	0.27	2.07
Forsterite -> Mg <sub>2</sub> SiO <sub>4</sub>	57	Est. 1%	(-2.37)	(4.53)
Jadeite -> NaAlSi <sub>2</sub> O <sub>6</sub>	14	Est. 1%	(-0.50)	(1.06)
Nepheline -> NaAlSiO <sub>4</sub>	13	Est. 1%	(-0.65)	(1.30)
Pyrope -> Mg <sub>3</sub> Al <sub>2</sub> Si <sub>3</sub> O <sub>12</sub>	76	Est. 1%	(-3.55)	(4.93)
Sanidine -> KAlSi <sub>3</sub> O <sub>8</sub>	10	Est. 1%	-1.91	2.80
Titanite -> CaTiSiO <sub>5</sub>	9	Est. 1%	-0.07	1.17
<b>Molecular Dynamics Simulations (0 ≤ P ≤ 40 GPa)</b>				
Angell and others (1987)	15	Est. 3%	(6.71)	(12.85)
Belonoshko and Dubrovinsky (1996)				
Mg <sub>2</sub> SiO <sub>4</sub>	58 <sup>n</sup>	Est. 3%	(-13.89)	(17.67)
Mg <sub>2</sub> Si <sub>2</sub> O <sub>6</sub>	30	Est. 3%	(-1.95)	(7.05)
Bryce and others (1999)				
NaAlO <sub>2</sub>	15	Est. 3%	(-9.35)	(11.98)
Na <sub>2</sub> Al <sub>2</sub> SiO <sub>6</sub>	6	Est. 3%	(-5.52)	(8.58)
NaAlSiO <sub>4</sub>	11	Est. 3%	1.12	3.05
NaAlSi <sub>2</sub> O <sub>6</sub>	23	Est. 3%	1.76	3.52
NaAlSi <sub>3</sub> O <sub>8</sub>	14	Est. 3%	1.93	3.15
Diefenbacher and others (1998)	16	Est. 3%	(73.0)	(132)

TABLE 1  
(continued)

Source	Number of data points	% std error in $\rho$ (data uncertainty)	% Systematic error in $\rho$ (model estimate) <sup>a</sup>	% std error in $\rho$ (model estimate)
Matsui (1996)				
Mg <sub>2</sub> Si <sub>2</sub> O <sub>6</sub>	5	Est. 3%	1.94	2.74
CaMgSi <sub>2</sub> O <sub>6</sub>	8	Est. 3%	1.54	2.23
CaAl <sub>2</sub> Si <sub>2</sub> O <sub>8</sub>	5	Est. 3%	0.33	3.41
CaSiO <sub>3</sub>	5	Est. 3%	4.26	1.45
Morgan and Spera (2001a, 2001b)	17	5%	3.62	5.12
Nevins and Spera (1998)	8	2.6%	1.57	2.64
Wasserman and others (1993)				
Mg <sub>2</sub> SiO <sub>4</sub>	2	Est. 3%	(4.47)	(4.79)
Mg <sub>2</sub> Si <sub>2</sub> O <sub>6</sub>	10	Est. 3%	(2.61)	(10.15)
Zhou and Miller (1997)				
Mg <sub>2</sub> SiO <sub>4</sub>	1	Est. 3%	(- 19.6)	
Mg <sub>2</sub> Si <sub>2</sub> O <sub>6</sub>	1	Est. 3%	(- 6.94)	
Mg <sub>3</sub> Si <sub>2</sub> O <sub>7</sub>	1	Est. 3%	(3.05)	

<sup>a</sup>Positive values indicate overestimation of the model density by the tabulated percentage of the average measured density.

<sup>b</sup>Conditions: 0.17–5 GPa; 1300–1600°C. Densities calculated by the author.

<sup>c</sup>Conditions: 1–10.1 GPa; 1400–2000°C. Densities calculated by the authors.

<sup>d</sup>Conditions: 1–11.5 GPa; 1415–2075°C. Densities calculated by the authors.

<sup>e</sup>Conditions: 5–14 GPa; 1250–1650°C. Densities calculated by the authors.

<sup>f</sup>Conditions: 12–16.3 GPa; 2200–2500°C. Densities calculated here from the equation of state of diamond provided by the authors.

<sup>g</sup>Conditions: 6–10 GPa; 1800–2000°C. Densities calculated here from the equation of state of diamond, forsterite and fayalite as provided by Ohtani and others (1998).

<sup>h</sup>Conditions: 7.4–20.5 GPa; 1890–1260°C. Densities calculated here from the equation of state of diamond, forsterite and fayalite as provided by the authors.

<sup>i</sup>Conditions: 0.5–3.5 GPa; 1360–1720°C. Densities calculated by the authors.

<sup>j</sup>Conditions: 8.1–22.1 GPa; 1870–2500°C. Densities calculated here from the equation of state of diamond, forsterite and fayalite as provided by Suzuki and others (1995).

<sup>k</sup>Conditions: 6.3–20.5 GPa; 1800–2570°C. Densities calculated here from the equation of state of diamond, forsterite and fayalite as provided by the authors.

<sup>l</sup>Average values are listed for shock compression studies. In the parameter optimization, a standard error estimated by the authors for each datum is used to weight residuals.

<sup>m</sup>Results enclosed in parentheses indicate that the dataset was not used as an active constraint in determining model parameters.

<sup>n</sup>Data points<sup>8</sup> from Belonoshko and Dubrovinsky (1996) are generated from their parameterized EOS for equal units of compression (0.005) over the pressure range 0–40 GPa.

constraints on the volumetric properties of iron-bearing melts. However, there is a complication in using these data that relates to the fact that the oxygen fugacity conditions of the experiments are unspecified, although they are generally assumed to correspond to reducing conditions. This complication leads to ambiguity in assessing the oxidation state of iron in the melt, and to uncertainty in ascribing variation in melt density to contributions from the three iron-bearing melt species: FeO, FeO<sub>1.3</sub>, and FeO<sub>1.5</sub> (Part II). In utilizing the Fe<sub>2</sub>SiO<sub>4</sub>, komatiite- and MORB-liquid data as well as the other Fe-bearing sink-float data as density constraints, the assumption is made that oxidation state conditions are sufficiently reducing so that iron is primarily present as FeO. This is a reasonable approximation for experiments conducted in graphite capsules at low pressure with oxygen fugacity conditions corresponding to the C-CO-

CO<sub>2</sub> buffer (Huebner, 1971; Kress and Carmichael, 1991) and should also be applicable to experiments conducted in Mo-capsules. As the reference pressure partial molar volumes of FeO<sub>1.3</sub> and FeO<sub>1.5</sub> are larger than that of FeO (Part II), at fixed oxygen fugacity increasing pressure should reduce any oxidized iron in the melt (Carmichael and Ghiorso, 1986) and the assumption should be further improved.

#### CALIBRATION

Combining sink-float, shock compression and fusion curve experimental constraints with molecular dynamics simulations in order to calibrate model EOS mixing parameters presents a number of challenges. First and foremost, each of the data sources generates a different kind of constraint: the sink-float experiments provide feasible *density bounds* subject to uncertainties in  $T$ ,  $P$  and the EOS of the solid marker, the molecular dynamics and shock-compression measurements provide *density estimates with an associated uncertainty*, and the fusion curve experimental  $P$ - $T$  brackets provide constraints (subject to uncertainties in  $T$  and  $P$ ) on the *pressure integral of the volume*. Data from each kind of study are subject to different intrinsic errors, and these differences must be accounted for in weighting residuals in the course of parameter calibration. Furthermore, a common objective function must be formulated for the whole optimization procedure if a stable and unbiased solution is to be obtained. In this section of the paper, the issue of generating an objective function for optimization is discussed first and then the problem of how to weight each data source is addressed.

#### *Objective Function for Parameter Optimization*

Sink-float density measurements provide bounds on melt density. These measurements are relatively easy to cast into an objective function for optimization of model parameters. If  $\Delta\rho^{l-s}$  is the calculated density difference between liquid and solid at the temperature and pressure conditions of the experiment, and if it is assumed that this difference is only a function of the model parameters of the liquid EOS, then the following residual functions ( $r_{static}$ ) may be defined:

$$r_{static} = \begin{cases} \Delta\rho^{l-s} & \rho^{liq} > \rho^{sol} \\ 0 & \rho^{liq} \leq \rho^{sol} \end{cases} \quad \text{if the index solid sinks} \quad (17a)$$

$$r_{static} = \begin{cases} 0 & \rho^{liq} \geq \rho^{sol} \\ \Delta\rho^{l-s} & \rho^{liq} < \rho^{sol} \end{cases} \quad \text{if the index solid floats} \quad (17b)$$

and

$$r_{static} = \Delta\rho^{l-s} \quad \text{if the index solid is neutrally buoyant} \quad (17c)$$

The residuals defined by equation (17) are assembled into an objective function (a weighted residual sum-of-squares) given by

$$\mathbf{X}_{static}^2 = \sum_i \left( \frac{r_{static,i}}{\sigma_{static,i}} \right)^2 \quad (18)$$

where  $\sigma_{static,i}$  is an estimate of the standard error associated with a particular measurement and the sum is over all experimental observations.

A residual function for optimizing molecular dynamics estimates of melt density is taken simply as the

$$r_{MD} = \rho^{calc} - \rho^{simulation} \quad (19)$$

A suitable objective function may be constructed from these residuals

$$X_{MD}^2 = \sum_i \left( \frac{r_{MD,i}}{\sigma_{MD,i}} \right)^2 \quad (20)$$

where as above,  $\sigma_{MD,i}$  is an estimate of the standard error associated with a particular result and the sum is over all data points computed by the molecular dynamics simulation.

Melt density estimates obtained from shock-compression studies are a bit more difficult to utilize as constraints in that the presumed temperature of the shock must be calculated and is dependent upon the adopted EOS. In treating these data previously (Part III) density and internal energy are fitted simultaneously for each experimental study, and temperature estimates are extracted along with model EOS parameter values. For calibration purposes in this paper, temperature estimates obtained in Part III are adopted and density alone is used to compute a model residual ( $r_{shock}$ )

$$r_{shock} = \rho^{calc} - \rho^{meas} \quad (21)$$

Model EOS parameters are optimized by minimizing a sum-of-squares equivalent to that specified for the sink-float density measurements and molecular dynamics simulations

$$X_{shock}^2 = \sum_i \left( \frac{r_{shock,i}}{\sigma_{shock,i}} \right)^2 \quad (22)$$

with appropriate estimates of measurement errors ( $\sigma_{shock,i}$ ).

The fusion curve data present a greater challenge. In order to combine sink-float, molecular dynamics and shock-compression density estimates with data defining  $P$ - $T$  brackets on mineral fusion curves, it is convenient to transform the latter into  $P$ - $T$  brackets on melt density. Simple convenience, however, is not the only motivation for this transformation, as the following discussion illustrates. An experimental bracket on a mineral fusion curve gives the magnitude and sign of the Gibbs free energy change of the solid-liquid melting reaction (Part III),

$$\Delta G = \Delta H_{P_r}^o - T\Delta S_{P_r}^o + \int_{P_r}^P V^{liq} dP - \int_{P_r}^P V^{sol} dP \quad (23)$$

where  $\Delta H_{P_r}^o$  and  $\Delta S_{P_r}^o$  are the enthalpy and entropy change of the melting reaction at  $T$  and  $P_r$ .  $\Delta G$  of equation (23) must be positive if the experimental results indicate that only solid is present, negative if only liquid is indicated, and zero if both liquid and solid appear to coexist in equilibrium at the specified  $T$  and  $P$ . These criteria motivate an algorithm for utilizing equation (23) to facilitate fitting of liquid EOS parameters from fusion curve data. A  $P$ - $T$  bracket residual ( $r_{fusion}$ ) is computed as follows:

$$r_{fusion} = \begin{cases} \Delta G & \Delta G < 0 \\ 0 & \Delta G \geq 0 \end{cases} \quad \text{if the experiment found all solid} \quad (24a)$$

$$r_{fusion} = \begin{cases} 0 & \Delta G \leq 0 \\ \Delta G & \Delta G > 0 \end{cases} \quad \text{if the experiment found all liquid} \quad (24b)$$

$$r_{fusion} = \Delta G \quad \text{if the experiment found two-phases} \quad (24c)$$

A least squares objective function is formed by summing the squares of these residuals over all observations,

$$\mathbf{X}_{fusion}^2 = \sum_i \left( \frac{r_{fusion,i}}{\sigma_{fusion,i}} \right)^2 \quad (25)$$

and this function is minimized with respect to model parameters of the EOS. Liquid EOS parameters fitted from fusion curve brackets via equations (24) and (25) necessarily weight higher-pressure data in favor of those at lower-pressure. This is because the integrand ( $V^{liq}$ ) of the volume integral contribution ( $\int_{P_r}^P V^{liq} dP$ ) to equation (23) is scaled by the pressure difference,  $P - P_r$ . An equivalent residual in Gibbs free energy at elevated pressure demands a more precise value of  $V$  (that is, density) than one at low pressure. As relative free energy change is the critical concern for accurate modeling of the fusion curve this issue is not of great importance if that is the objective of the exercise, but if it is desired to interpret the fusion curve brackets in terms of *uniform errors* in implied melt density regardless of the pressure range of the experiments, then computation of residuals according to equation (24) is inappropriate. Thus, there is strong motivation for transformation of fusion curve brackets from constraints on Gibbs free energy to constraints on density.

Application of the mean-value theorem to the integral  $\int_{P_r}^P V^{liq} dP$  gives the result

$$\int_{P_r}^P V^{liq} dP = V_{P'}^{liq} (P - P_r) \quad (26)$$

where  $P'$  is some pressure in the interval  $P - P_r$  and the liquid volume ( $V_{P'}^{liq}$ ) is evaluated at this pressure. Assuming that the Gibbs free energy residual as defined by equation (24) can be entirely ascribed to the liquid EOS, then

$$\Delta G = \Delta V_{P'}^{liq} (P - P_r) \quad (27)$$

where  $\Delta V_{P'}^{liq}$  represents an equivalent residual in liquid volume. Writing the volume change in equation (27) as

$$\Delta V_{P'}^{liq} = \frac{M}{\rho_1} - \frac{M}{\rho_2} \quad (28)$$

where  $M$  is the gram-formula-weight and  $\rho$  density of melt, some rearrangement gives

$$\Delta V_{P'}^{liq} = \frac{M \Delta \rho_{res}}{\bar{\rho}^2} \quad (29)$$

where  $\Delta \rho_{res}$  is the equivalent residual melt density and  $\bar{\rho}$  is the average density of the liquid (at the temperature,  $T$  and pressure,  $P'$ , which is approximated as the average pressure over the experimental interval). Combining equations (27) and (29) allows equation (24) to be rewritten as

$$r_{fusion} = \begin{cases} \frac{\Delta G \bar{\rho}^2}{M(P - P_r)} & \Delta G < 0 \\ 0 & \Delta G \geq 0 \end{cases} \quad \text{if the experiment found all solid} \quad (30a)$$

$$r_{fusion} = \begin{cases} 0 & \Delta G \leq 0 \\ \frac{\Delta G \bar{\rho}^2}{M(P - P_r)} & \Delta G > 0 \end{cases} \quad \text{if the experiment found all liquid} \quad (30b)$$

$$r_{fusion} = \frac{\Delta G \bar{\rho}^2}{M(P - P_r)} \quad \text{if the experiment found two-phases} \quad (30c)$$

The residuals defined by equation (30) have units of density and are no longer weighted to preferentially accommodate high-pressure data. The objective function defined by equation (25) may still be utilized with these revised definitions of  $r_{fusion}$ .

Equations (18), (20), (22) and (25) can be combined to formulate a global objective function from which model EOS parameters may be optimized. In stipulating this function, it is convenient to distinguish individual data sources within each type of data, and to ascribe a weight ( $0 \leq w \leq 1$ ) to each data source. Indexing individual data sources on  $j$  and using the index  $i$  to denote experimental results from that source, the final objective function is

$$\begin{aligned} X^2 = \sum_j w_{static,j} \sum_i^{n_j} \left( \frac{r_{static,i,j}}{\sigma_{static,i,j}} \right)^2 + \sum_j w_{MD,j} \sum_i^{n_j} \left( \frac{r_{MD,i,j}}{\sigma_{MD,i,j}} \right)^2 + \sum_j w_{shock,j} \sum_i^{n_j} \left( \frac{r_{shock,i,j}}{\sigma_{shock,i,j}} \right)^2 \\ + \sum_j w_{fusion,j} \sum_i^{n_j} \left( \frac{r_{fusion,i,j}}{\sigma_{fusion,i,j}} \right)^2 \quad (31) \end{aligned}$$

In the next section the attribution of weights and standard errors of the various data sources is developed.

#### *Weights and Standard Errors of Data Sources*

Uncertainties in melt densities reported in shock-compression studies are adopted as an approximation of the standard error of measurement. The *average* relative uncertainty in each of the data sources used here is listed in table 1. The values range from less than 1 percent to approximately 3 percent relative error.

Uncertainties in densities derived from molecular dynamics simulations are assumed to be about 3 percent, unless better estimates are reported. For simulations conducted at low pressure (0-5 GPa), a 3 percent uncertainty is probably an underestimation of the error, because long run times are required to develop good fluctuation statistics under these conditions. On the other hand, a 3 percent uncertainty is probably very conservative for high-pressure simulations, where shorter run times are permissible and where simulations with alternate descriptions of atomic forces result in density estimates that differ by less than one or two percent (Part III).

Uncertainty estimates for the sink-float density brackets are much more difficult to obtain. Typically, an error estimate on the location of a density bracket of about 1 percent is reported. But, these estimates are largely derived from measurement errors in  $T$  and  $P$  propagated through the EOS for the index mineral density marker. Experimental difficulties such as convection and non-uniform temperatures in the charge, short experimental run times (many of the multianvil experiments are less than a minute in duration), and movement of the marker during ramp-up and quenching will serve to increase the uncertainty on the location of the density brackets. Knoche and Luth (1996) made a careful study of these issues in the system  $\text{Na}_2\text{O-Al}_2\text{O}_3\text{-SiO}_2$  and concluded that uncertainties in the location of density brackets are likely on the order of 3 percent. A relative error of this size may very well be applicable to the other studies, but a counterargument can be made that the internal consistency of a series of measurements that yield smooth variation of melt density with either  $T$  or  $P$  (for example, the results of Agee, 1992a, 1992b on  $\text{Fe}_2\text{SiO}_4$  liquid) would not resolve a coherent pattern if the location of the brackets were this uncertain. Of course, the internal consistency of measurements in a single study might simply reflect the precision of the experimental procedure and not the accuracy of the measurement. For the purposes of adopting a standard error to use in equation (31) for the sink-float density data sources, an average error estimate of 1 percent in relative density is assumed except for the study of Knoche and Luth (1996), where the reported density

range is taken. Most likely, adoption of a 1 percent uncertainty will result in preferential weighting of the sink-float density brackets over the other data sources in the final optimization. Preferential weighting in favor of the sink-float results is not inconsistent with the principal objective of the calibration effort, as the sink-float experiments span the liquid composition range of primary interest.

Standard errors in density estimates derived from analysis of the fusion curve data (eq 32) are also difficult to assess. The path of the fusion curve in  $T$ - $P$  space is critically sensitive to the density difference of the solid and liquid phase ( $\Delta\rho = \rho^{liq} - \rho^{sol}$ ) and an error of moderate size in  $\Delta\rho$  can result in considerable uncertainty in the calculated  $T \pm \varepsilon_T$ ,  $P \pm \varepsilon_P$  coordinates. A relationship can be derived to relate  $\Delta\rho$  to  $\varepsilon_T$  and  $\varepsilon_P$  using the thermodynamic expression (eq 23) that defines the equilibrium fusion curve

$$0 = \Delta H_{P_r} - T\Delta S_{P_r} + \int_{P_r}^P \Delta V dP = \Delta H_{P_r} - T\Delta S_{P_r} - M \int_{P_r}^P \frac{\Delta\rho}{\rho^{liq}\rho^{sol}} dP \quad (32)$$

Examining first the uncertainty in  $\Delta\rho$  arising from an uncertainty in  $T$ , thermodynamic equilibrium requires that equation (32) hold for the  $(\Delta\rho, T)$  pair as well as the perturbation  $(\Delta\rho + \varepsilon_{\Delta\rho}, T + \varepsilon_T)$  from which

$$0 = \left[ \Delta H_{P_r} - (T + \varepsilon_T)\Delta S_{P_r} - M \int_{P_r}^P \frac{\Delta\rho + \varepsilon_{\Delta\rho}}{\rho^{liq}\rho^{sol}} dP \right] - \left( \Delta H_{P_r} - T\Delta S_{P_r} - M \int_{P_r}^P \frac{\Delta\rho}{\rho^{liq}\rho^{sol}} dP \right) \quad (33)$$

which simplifies to

$$0 = -\varepsilon_T\Delta S_{P_r} - M \int_{P_r}^P \frac{\varepsilon_{\Delta\rho}}{\rho^{liq}\rho^{sol}} dP \approx -\varepsilon_T\Delta S_{P_r} - M \frac{\varepsilon_{\Delta\rho}}{\rho^{liq}\rho^{sol}} (P - P_r) \quad (34)$$

or equivalently

$$\frac{\varepsilon_{\Delta\rho}}{\rho^{liq}} \approx \frac{\varepsilon_T \rho^{sol} \Delta S_{P_r}}{M(P - P_r)} \quad (35)$$

Ascribing the error in  $\Delta\rho$  entirely to the liquid phase, the left-hand-side of equation (35) provides an estimate of the relative error in  $\rho^{liq}$  implied by an absolute error of  $\varepsilon_T$  in location of the fusion curve. Similarly, an uncertainty in  $\Delta\rho$  arising from an uncertainty in  $P$  follows from

$$0 = \left[ \Delta H_{P_r} - T\Delta S_{P_r} - M \int_{P_r}^{P+\varepsilon_P} \frac{\Delta\rho + \varepsilon_{\Delta\rho}}{\rho^{liq}\rho^{sol}} dP \right] - \left( \Delta H_{P_r} - T\Delta S_{P_r} - M \int_{P_r}^P \frac{\Delta\rho}{\rho^{liq}\rho^{sol}} dP \right) \quad (36)$$

which simplifies to

$$0 = -M \int_{P_r}^P \frac{\varepsilon_{\Delta\rho}}{\rho^{liq}\rho^{sol}} dP - M \int_{P_r}^{P+\varepsilon_P} \frac{\Delta\rho + \varepsilon_{\Delta\rho}}{\rho^{liq}\rho^{sol}} dP \approx -M \frac{\varepsilon_{\Delta\rho}}{\rho^{liq}\rho^{sol}} (P - P_r) - M \frac{\Delta\rho + \varepsilon_{\Delta\rho}}{\rho^{liq}\rho^{sol}} \varepsilon_P \quad (37)$$

and yields the relation

$$\frac{\varepsilon_{\Delta\rho}}{\rho^{liq}} \approx \frac{-\varepsilon_P \Delta\rho}{\rho^{liq} [(P - P_r) - \varepsilon_P]} \quad (38)$$

Inserting typical values ( $\epsilon_T = 50^\circ\text{C}$ ,  $M = 150$  gm/mol,  $\rho^{sol} = 3$  gm/cc, and  $\Delta S_p = 60$  J/mol) into equation (35) gives  $\frac{\epsilon_{\Delta\rho}}{\rho^{liq}} \approx \frac{10^{-3}}{P - P_r}$ , with pressure measured in GPa. Using equation (38), typical values ( $\epsilon_p = 0.01$  GPa,  $\Delta\rho = 0.3$  gm/cc,  $\rho^{liq} = 3$  gm/cc) for moderate to high-pressure yield  $\frac{\epsilon_{\Delta\rho}}{\rho^{liq}} \approx \frac{10^{-3}}{P - P_r}$ . A larger pressure uncertainty in multi-anvil experimental studies may increase the latter value by an order of magnitude. This analysis suggests that a *conservative* estimate in the relative error of  $\Delta\rho$  derived from typical fusion curve measurements is on the order of 1 percent. This value will be adopted for optimization of fusion curve data via equation (31).

Relative importance of the various data sets is stipulated in the objective function specified above (eq 31) by the weighting factors ( $w_{static,i}$ ,  $w_{MD,i}$ ,  $w_{shock,i}$ ,  $w_{fusion,i}$ ). These factors are meant to provide a means of minimizing the inconsistency between various data sources and to give greater stability to the optimization problem. Although a more sophisticated fractional weighting scheme could be adopted, in this analysis the weights on the data sources are assigned either a value of zero or one, for example a data set is excluded or included in the optimization of model EOS parameters.

All of the sink-float experiments are included as equal and active constraints on the parameter regression. Inclusion or exclusion of the other data sets is motivated entirely from the analysis presented in Part III. All of the shock compression studies are included, with the exception of the work of Rigden and others (1989) on  $\text{CaAl}_2\text{Si}_2\text{O}_8$  liquid. These data are excluded because it is shown in Part III that the Hugoniot  $\rho$ - $T$ - $P$  relations are inconsistent with the molecular dynamics studies of Matsui (1996), Nevins and Spera (1998) and Morgan and Spera (2001a, 2001b). Density constraints derived from the fusion curves of forsterite and enstatite are also excluded as well as the molecular dynamics studies on  $\text{MgO}$ - $\text{SiO}_2$  binary liquids with molar ratios of  $\text{MgO}/\text{SiO}_2 \geq 1$ . This choice is made because modeling these liquids (Part III) requires modification of the reference pressure EOS parameter values from Part II, indicating a non-linear volume of mixing term that is absent from the reference pressure formulation. Similarly, molecular dynamics data on molten silica and fusion curve data on the silica minerals are excluded because the volumetric properties of pure  $\text{SiO}_2$  liquid are dominated by configurational contributions (Part I) and partial molar properties derived from mixed liquids (Part II) do not extrapolate well to the pure endmember. Data on the fusion curves of albite, jadeite and nepheline are not included in the optimization. These data sets provide ambiguous constraints (albite, Part III) or are dependent on derived temperatures of fusion (jadeite, Part III) or mineral volumes (nepheline, Part III). The volumetric properties of  $\text{NaAlSiO}_4$ ,  $\text{NaAlSi}_2\text{O}_6$ , and  $\text{NaAlSi}_3\text{O}_8$  melts from the molecular dynamics studies of Bryce and others (1999) are included, but compositions investigated by these authors with molar ratios of  $\text{NaAlO}_2/\text{SiO}_2 < 1$  are excluded because they fall outside the reference pressure calibration. The molecular dynamics simulations of Diefenbacher and others (1998) give a reference pressure volume inconsistent with the calibration of Part II and these data are also removed as active constraints. Lastly, because the configurational contribution to the volume of liquid  $\text{Mg}_3\text{Al}_2\text{Si}_3\text{O}_{12}$  at pressure is not known, the fusion curve data for pyrope is not included in the parameter optimization. In summary, all the included and excluded data sets are listed in table 1 and indicated accordingly.

Only molecular dynamics results generated over the pressure interval zero to 40 GPa are included in the parameter optimization. While the functional form of the EOS is demonstrably capable (Part III) of modeling simulation results to pressures in excess of 100 GPa, the compositional range over which such high pressure information is available is very restricted. Rather than bias the mixing parameter estimation through the inclusion of selected high-pressure constraints, a cut-off pressure is adopted to

make the molecular dynamics studies span a pressure interval comparable to the shock compression work.

#### *Configurational Contributions to the Volume*

One of the principal conclusions that emerges from the analysis of Part III is that proper calibration of EOS parameters at elevated pressure requires explicit provision for volumetric effects associated with configurational collapse related to changing oxygen coordination number (CN) of Si and Al with pressure. Molecular dynamics simulations provide an excellent means of quantitatively assessing the effect of  $T$ ,  $P$ , and composition on melt structure and results of these simulations establish an explicit relationship between melt structure and derived macroscopic thermodynamic properties, like density. A simple ideal associated solution model is developed in Part I and applied in Part III that is very successful in modeling density variation in liquids that undergo significant structural changes with pressure. This thermodynamic model accounts for configurational effects and incorporates the proposed liquid EOS to describe the vibrational contribution to the Gibbs free energy of the liquid.

To apply the thermodynamic treatment developed in Part I and Part III to the problem at hand is complicated by the lack of direct information on the CN of Si and Al in the sink-float experimental liquids. Some approximation must be adopted. In Part III CN-speciation models are developed for  $\text{CaMgSi}_2\text{O}_6$  liquid from the molecular dynamics studies of Matsui (1996), for  $\text{NaAlO}_2\text{-SiO}_2$  liquids from the work of Bryce and others (1999), for  $\text{CaAl}_2\text{Si}_2\text{O}_8$  liquid from the work of Morgan and Spera (2001a, 2001b) and Nevins and Spera (1998), and for  $\text{Mg}_2\text{Si}_2\text{O}_6$  liquid from the work of Kubicki and Lasaga (1991) and Wasserman and others (1993). A model for  $(\text{CaMgSi}_2\text{O}_6)_{0.64}\text{-}(\text{CaAl}_2\text{Si}_2\text{O}_8)_{0.36}$  liquid is developed by combining formulations for the endmembers, and this approximation is applied in Part III to the MORB-liquid experiments of Rowan (ms, 1993). The CN-speciation model for  $\text{Mg}_2\text{Si}_2\text{O}_6$  is adopted for shock compression results on a komatiitic liquid (Miller and others, 1991), as this composition is to a first approximation  $\sim 80$  mol percent  $(\text{Mg,Fe})_2\text{Si}_2\text{O}_6$ . The CN-speciation models developed in Part III are applied here to compute density residuals for each data set (eq 31). The use of these models means that the parameter values calibrated in this paper apply to the “vibrational” reference state of the liquid, where all Si and Al are in four-fold coordination with oxygen. Equation (43) of Part III must be used to correct the volume calculated from this parameterization in order to account for the effects of higher coordination states of Si and Al. For sink-float experiments on ultramafic liquids (Agee and Walker, 1988, 1993; Suzuki and others, 1995, 1998; Ohtani and others, 1995, 1998; Smith and Agee, 1997; Suzuki and Ohtani, 2003), the CN-speciation model developed in Part III for  $\text{Mg}_2\text{Si}_2\text{O}_6$  liquid is adopted. For experiments on basaltic liquids (Ohtani and Maeda, 2001), the Part III model for  $(\text{CaMgSi}_2\text{O}_6)_{0.64}\text{-}(\text{CaAl}_2\text{Si}_2\text{O}_8)_{0.36}$  liquid is used. The lunar composition liquids studied by Circone and Agee (1996) and Smith and Agee (1997) are treated with the assumption that Si and Al remains largely in [IV] coordination; experimental results on  $\text{Fe}_2\text{SiO}_4$  liquid (Agee 1992a, 1992b) and sodium silicate liquid (Knoche and Luth, 1996) are dealt with similarly. It would be desirable to have a better notion of the variation of (Si, Al) CN with  $T$ ,  $P$ , and composition for the sink-float liquids. If the CN-speciation behavior of  $\text{Mg}_2\text{Si}_2\text{O}_6$  and  $\text{CaMgSi}_2\text{O}_6$  liquids are reasonable approximations for komatiite and peridotite melts, then the effect of higher-CN states of Si and Al on melt density is probably not significant over the pressure range of the experimental studies listed in table 1. On the other hand, if MORB liquids exhibit (Si, Al) CN transformations similar to  $(\text{CaMgSi}_2\text{O}_6)_{0.64}\text{-}(\text{CaAl}_2\text{Si}_2\text{O}_8)_{0.36}$  (Part III), then under the experimental conditions of Ohtani and Maeda (2001), close to 65 percent of the Si and Al would be in five-fold coordination with respect to oxygen, implying an approximate density increase of  $\sim 6$  percent (Part III) over the equivalent (Si,Al) [IV]-density. This is

a significant effect that begs for verification by physical or computer experimentation. In the absence of a more rigorous alternative, the best that can be done is to attempt an internally consistent analysis and evaluate the assumptions regarding CN-speciation in the postmortem of the parameter optimization by examining systematic relations in model residuals.

#### Analysis and Discussion

Optimal mixing parameters ( $\bar{v}_{2,i}$ ,  $\bar{v}_{3,i}$ , and  $\bar{v}_{4,i}$ ) are obtained by minimizing the objective function defined by equation (31) using data sources listed in table 1. Care must be taken in performing this minimization so that the EOS (eq 1) does not develop a singularity, which can occur if parameter estimates for some bulk composition generate numerical values for the “ $a$ ” and “ $b$ ” terms in equation (1) that render positive real roots for the quadratic polynomial

$$1 + a(P - P_r) + b(P - P_r)^2 = 0 \quad (39)$$

While it is not possible to specify bounds on the  $\bar{v}_{2,i}$ ,  $\bar{v}_{3,i}$ , and  $\bar{v}_{4,i}$  that prevent the existence of any positive root of equation (39) over the whole range of applicable liquid compositions, it is possible to establish criteria that prevent the generation of positive real roots for specific liquid compositions. A method that translates these criteria into a mathematical expression that may be used as a bound constraint on optimization of mixing parameters is developed in the Appendix. This method is applied to all of the bulk compositions from all the experimental sources listed in table 1. The procedure generates a large number of non-linear inequality bounds that constrain the optimization path for the numerical routine that seeks the minimum of the objective function. The Solver™ routine from MS Excel™ is used to implement this bounded minimization problem.

Optimized model parameters are reported in table 2. Average percent errors associated with model recovery of experimentally determined densities or density bounds are reported in table 1 as “% std error in  $\rho$  (model estimate).” This quantity is

computed as the standard error of the residuals for that data set ( $\sigma = \sqrt{\sum_i^n r_i^2/n}$ )

divided by the average density of liquids in that set ( $\bar{\rho}$ ) and expressed as a percentage (that is  $\frac{100\sigma}{\bar{\rho}}$ ). The column labeled “% Systematic error in  $\rho$  (model estimate)” is the

systematic displacement the data set exhibits with respect to the global residual mean. This quantity is computed as the average of the residuals for that data set ( $\bar{r}$ ) divided by the average density of liquids in that set and expressed as a percentage (that is  $\frac{100\bar{r}}{\bar{\rho}}$ ).

Positive values indicate that the model systematically overestimates melt density, while negative values denote a systematic underestimation of melt density. The quantity listed as “% std error in  $\rho$  (data uncertainty)” in column three of table 1 is the reported or estimated uncertainty in melt density for that data set. It is a measure of precision, which may or may not reflect the accuracy of the observation(s). It is most appropriate to compare this quantity to the average % error *corrected for the local mean of residuals*, which may be computed from tabulated values in columns four and five using the

formula  $\sqrt{\left(\frac{100\sigma}{\bar{\rho}}\right)^2 - \left(\frac{100\bar{r}}{\bar{\rho}}\right)^2}$ . By correcting for the local residual mean, the systematic offset in the residuals is removed and the dispersion of model residuals can be compared directly to the expected dispersion of the measurements. Numbers that are in parentheses in table 1 reflect statistics computed for data sets *that are not included as active constraints in parameter estimation*.

TABLE 2  
Recommended parameter values for the adopted EOS

Oxide	Source: Part II				Source: this paper			
	$\bar{v}_{0,i}$ (cc/mol)	$\frac{\partial \bar{v}_{0,i}}{\partial T} \times 10^3$ (cc/mol-K)	$c_i$ (m/sec)	$\frac{\partial c_i}{\partial T} \times 10^3$ (m/sec-K)	$MW_i$ (gm/mol)	$\bar{v}_{2,i} \equiv \frac{\partial^2 \bar{v}_{0,i}}{\partial p^2}$ (cc/mol-GPa <sup>2</sup> )	$\bar{v}_{3,i} \equiv \frac{\partial^3 \bar{v}_{0,i}}{\partial p^3}$ (cc/mol-GPa <sup>3</sup> )	$\bar{v}_{4,i} \equiv \frac{\partial^4 \bar{v}_{0,i}}{\partial p^4}$ (cc/mol-GPa <sup>4</sup> )
SiO <sub>2</sub>	26.710	1.007	2321.75	399.34	60.0848	0.21995	0.010220	-0.00025985
TiO <sub>2</sub>	23.448	6.807	1693.60	811.99	79.8988	0.059857	0.10350	-0.054133
Al <sub>2</sub> O <sub>3</sub>	37.616	-0.6490	2738.35	503.94	101.9612	0.15738	-0.030193	0.0091947
FeO	13.895	1.532	2399.53	-107.26	71.8464	0.22771	-0.12968	0.060629
MgO	12.015	2.887	3349.96	275.64	40.3114	-0.025979	0.045354	-0.037501
CaO	16.671	3.143	3967.42	-205.26	56.0794	0.28439	-0.18258	0.043285
Na <sub>2</sub> O	29.117	6.077	3080.69	-2167.6	61.979	3.4298	-0.58834	-2.3510
K <sub>2</sub> O	46.401	10.43	1682.35	-2344.1	94.2034	21.300 <sup>1</sup>	-31.307	32.004

<sup>1</sup>High-pressure EOS parameters for the K<sub>2</sub>O component are very poorly constrained. See text.

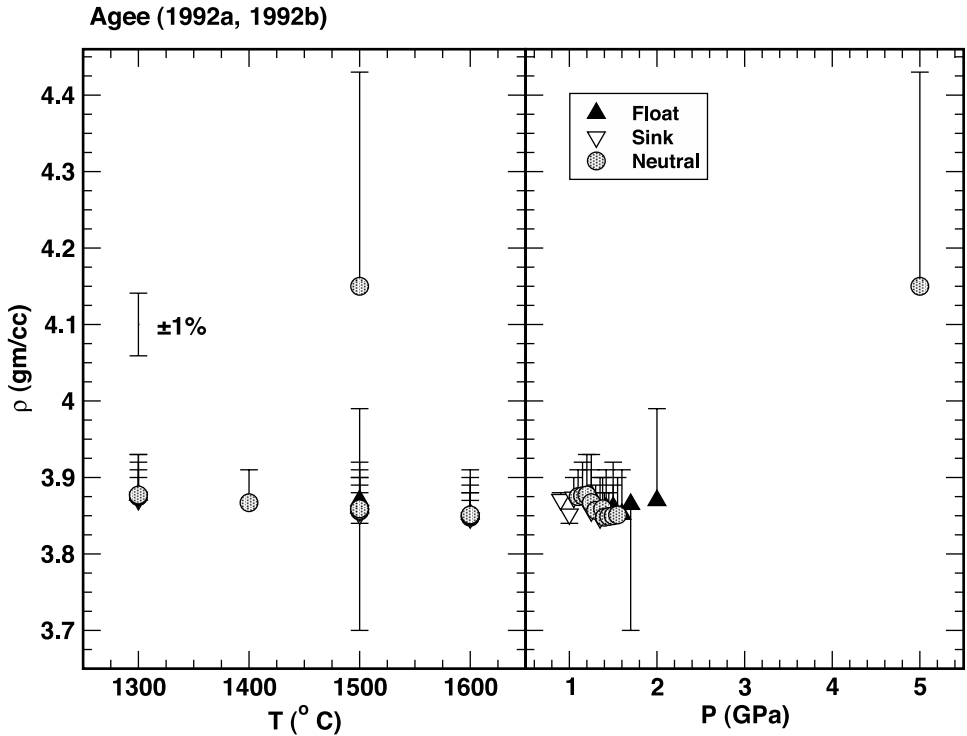


Fig. 1. Analysis of sink-float experimental data of Agee (1992a, 1992b) on  $\text{Fe}_2\text{SiO}_4$  composition liquids using ruby as a density marker. Density is reported in units of  $\text{grams}/\text{cm}^3$  and is plotted on the ordinate; temperature in  $^\circ\text{C}$  and pressure in GPa are plotted on the abscissa in the left and right panels, respectively. Upward pointing filled triangles denote experimental conditions where the index mineral floats in the liquid, unfilled triangles denote experimental conditions where the index mineral sinks in the liquid; the triangles are plotted at the calculated density of the mineral at the  $T$  and  $P$  of the experiment. Each triangle is connected by a straight line that terminates with a horizontal bracket plotted at a density calculated from the model EOS. Filled circles represent experimental conditions where the index mineral is neutrally buoyant in the liquid. An uncertainty bracket of  $\pm 1\%$  is provided for reference.

The table 1 entries that appear in columns four and five for the sink-float experiments represent density estimates that *violate* experimentally determined brackets and that *deviate* from neutral buoyancy measurements. For example, in the study of Agee and Walker (1988, 1993) on olivine floatation/sinking in komatiitic and peridotitic melts, the average melt density is  $\sim 3.25 \text{ gm}/\text{cc}^3$  and therefore the standard error bracket violation is on the order of  $\sim 0.045 \text{ gm}/\text{cc}^3$  (1.37% of 3.25). The systematic displacement of these data is  $\sim 0.028 \text{ gm}/\text{cc}^3$  (0.85% of 3.25) from the mean. The standard deviation bracket violation corrected for the local mean of residuals is 1.07% ( $\sqrt{1.37^2 - 0.85^2}$ ) or  $\sim 0.035 \text{ gm}/\text{cc}^3$  (1.07% of 3.25).

Model recovery of the sink-float data is examined in figures 1 through 9. Recovery of the shock compression Hugoniot is displayed in figure 10. The upper-bound density brackets of Agee and Walker (1988, 1993) are systematically overestimated by the model (fig. 2A and 2B) whereas similar compositions (though on average, less Fe-rich) studied by Ohtani and others (1995, 1998), Suzuki and Ohtani (2003), and Suzuki and others (1995, 1998) (figs. 8 and 9) show no systematic trends. Perhaps this discrepancy gives some measure of inter-laboratory error, which can be inferred to be on the order of 1 percent. If the *accuracy* of the sink-float experiments is at the 3 percent level (Knoche and Luth, 1996), then no disagreement exists between the

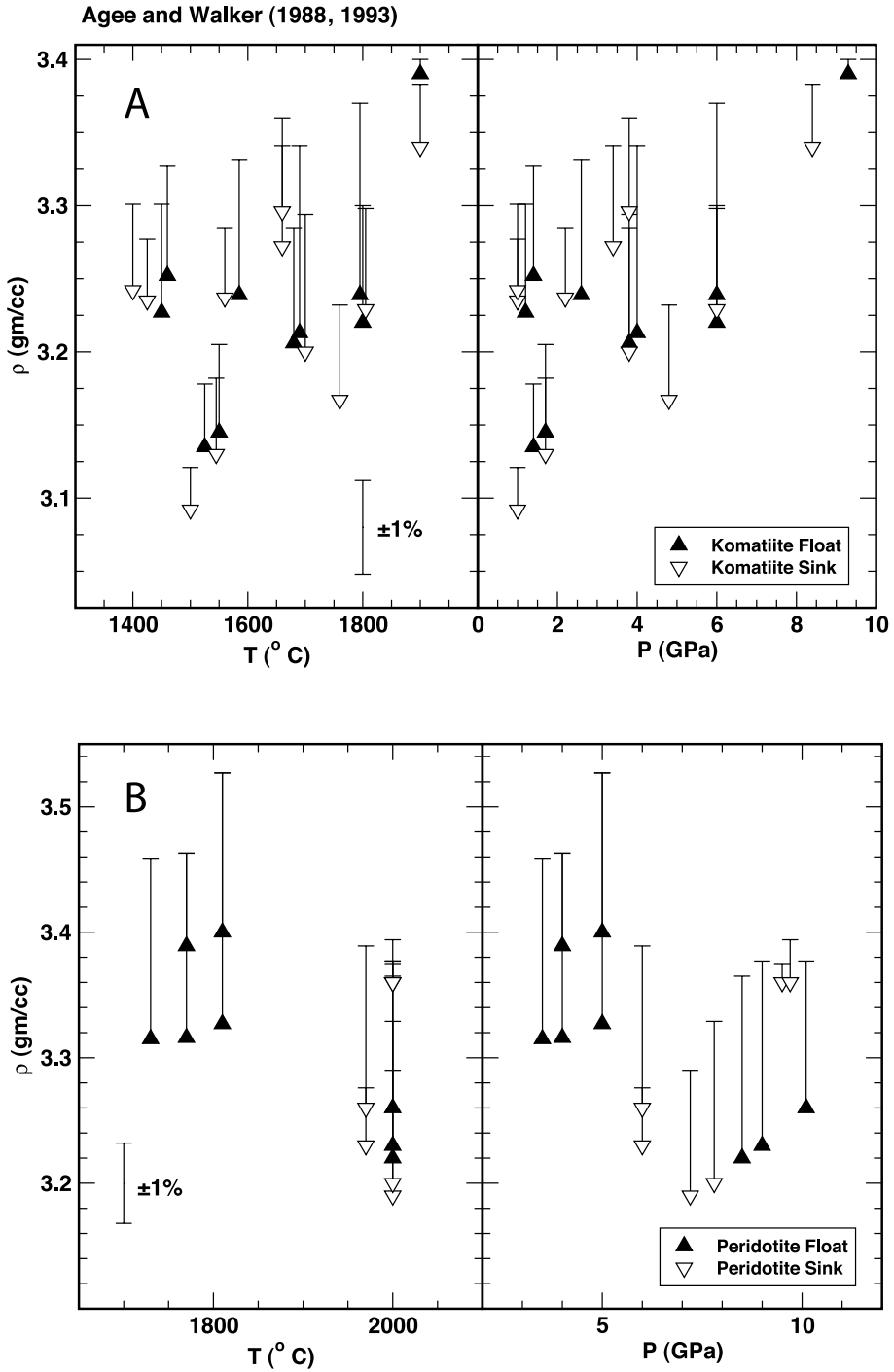


Fig. 2. Analysis of the sink-float experimental data of Agee and Walker (1993, 1998) on komatiitic and peridotitic composition liquids using olivine as a density marker. Symbol usage, axes content and labels follows figure 1. An uncertainty bracket of  $\pm 1\%$  is provided for reference. (A) Komatiite liquid experiments. (B) Peridotite liquid experiments.

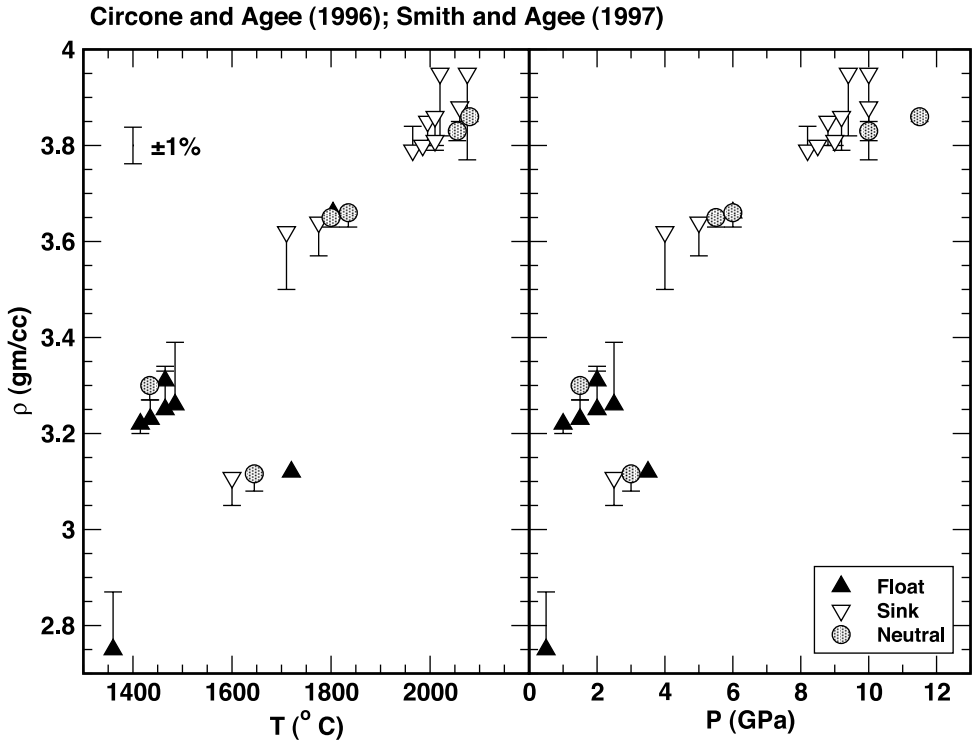


Fig. 3. Analysis of sink-float experimental data of Circone and Agee (1996) and Smith and Agee (1997) on lunar liquid compositions. Data points plotting at densities greater than 3.2 are from experiments on high-Ti basaltic liquids (Apollo 14 “black-glass” composition melts). Lower density data are from low-Ti basaltic liquids. Olivine, garnet and corundum were used as density markers in these experiments. Symbol usage, axes content and labels as in figure 1. An uncertainty bracket of  $\pm 1\%$  is provided for reference.

various sink-float studies on ultramafic liquids. As noted in Part III, the sink-float experiments of Agee (1992a, 1992b) on  $\text{Fe}_2\text{SiO}_4$  liquid are at odds with the shock compression studies of Chen and others (2002) and this explains the small systematic offsets of these two data sets; the 3.5 percent overestimation of the density of the datum of Agee (1992a) at 5 GPa (fig. 1) illustrates this inconsistency with the  $\text{Fe}_2\text{SiO}_4$  Hugoniot (fig. 10).

Recovery of the shock-compression  $\rho$ - $P$  constraints is excellent at  $P < 15$  GPa for the komatiitic liquids studied by Miller and others (1991), and above this pressure the model density is underestimated by as much as 2 percent at 35 GPa, which may be an indication that the CN-speciation model adopted for this liquid underestimates (Si, Al) in five-fold co-ordination at elevated pressure. Recovery of the shock compression, fusion curve and molecular dynamics results for  $\text{CaMgSi}_2\text{O}_6$  liquid are comparable to the fits obtained in Part III. Shock-compression constraints on  $\text{CaAl}_2\text{Si}_2\text{O}_8$  liquid were excluded from the calibration in favor of densities estimated from molecular dynamics studies, and this is reflected in the recovery of the Hugoniot of Rigden and others (1989), where the model overestimates the density by about 6 percent. The model Hugoniot for  $(\text{CaMgSi}_2\text{O}_6)_{0.64}(\text{CaAl}_2\text{Si}_2\text{O}_8)_{0.36}$  liquid again suggests an underestimation of CN  $>$  IV for (Si,Al) at high pressure.

Recovery of the shock compression data of Rowan (ms, 1993) is very disappointing and demonstrates an inconsistency between these measurements on MORB liquid and

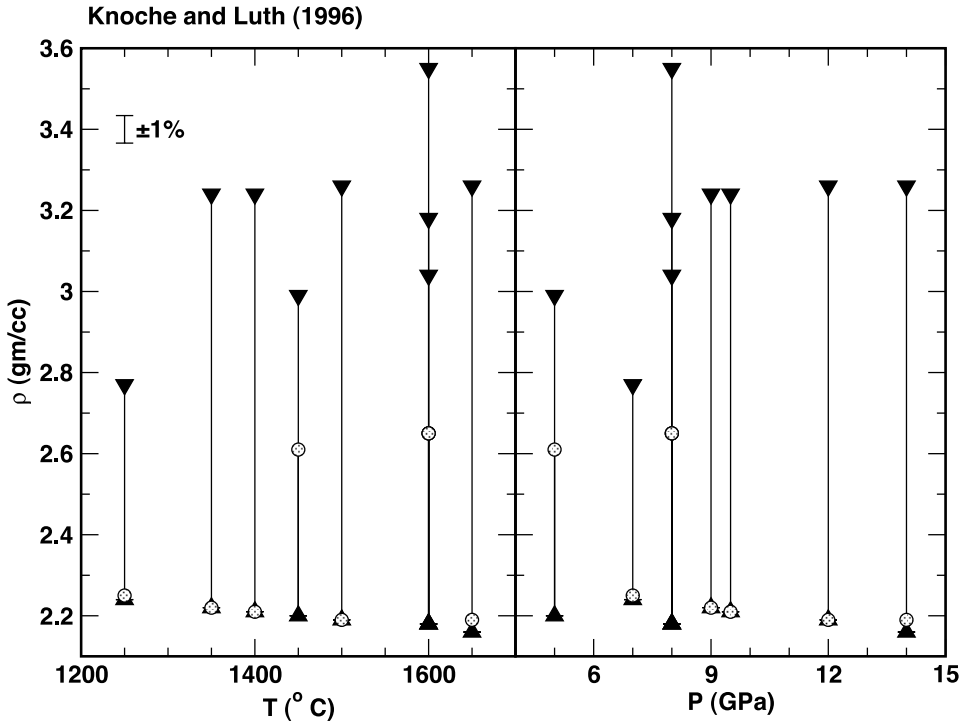


Fig. 4. Analysis of sink-float experimental data of Knoche and Luth (1996) on  $\text{Na}_2\text{O-SiO}_2$  composition melts using spinel, forsterite, andularia and quartz as density markers. Brackets terminated by downward and upward pointing filled triangles limit the range of permissible density values admissible by the experimental data. Filled circles are plotted at a density calculated from the liquid EOS. An uncertainty bracket of  $\pm 1\%$  is provided for reference; note that a 1% uncertainty is considerably less than the experimentally determined brackets. Axes content and labels follows figure 1.

the work of Ohtani and Maeda (2001; MORB liquid) and Smith and Agee (1997; a low Ti basaltic liquid). For example, Ohtani and Maeda (2001) bracket a density of  $\sim 3.56 \text{ gm/cm}^3$  for MORB at  $2200^\circ\text{C}$  and 15 GPa while Rowan (ms, 1993) measures a density of  $\sim 3.74 \text{ gm/cm}^3$  under essentially the same  $P$ - $T$  conditions ( $T$  estimates from Part III). Taken by themselves, the Hugoniot data from Rowan (ms, 1993) can be modeled in an internally consistent fashion (Part III; dashed curve in figure 10), but what is significant is the inconsistency that is revealed when these data are examined in combination with the other data sets. The data of Ohtani and Maeda (2001) on MORB are generally consistent with the sink-float experimental results on ultramafic compositions, so the inconsistency is not rooted in the extrapolation of the parameter mixing model to MORB-like liquids.

Model recovery of the molecular dynamics results of Bryce and others (1999) on  $\text{NaAlSiO}_4$ ,  $\text{NaAlSi}_2\text{O}_6$ , and  $\text{NaAlSi}_3\text{O}_8$  is at the expected level of precision. When model parameters are utilized to calculate densities of liquids along the fusion curves of nepheline, jadeite and albite, these data are recovered even though they were not used in parameter optimization. Extrapolation of the model calibration to more silica poor compositions along the  $\text{NaAlO}_2\text{-SiO}_2$  join and to  $\text{Na}_2\text{Si}_4\text{O}_9$  liquids fails (table 1). As anticipated, the model does not recover the fusion curves or the molecular dynamics densities of melts along the  $\text{MgO-SiO}_2$  binary join. This failure is consistent with the analysis of these data in Part III, where it is shown that the reference-pressure

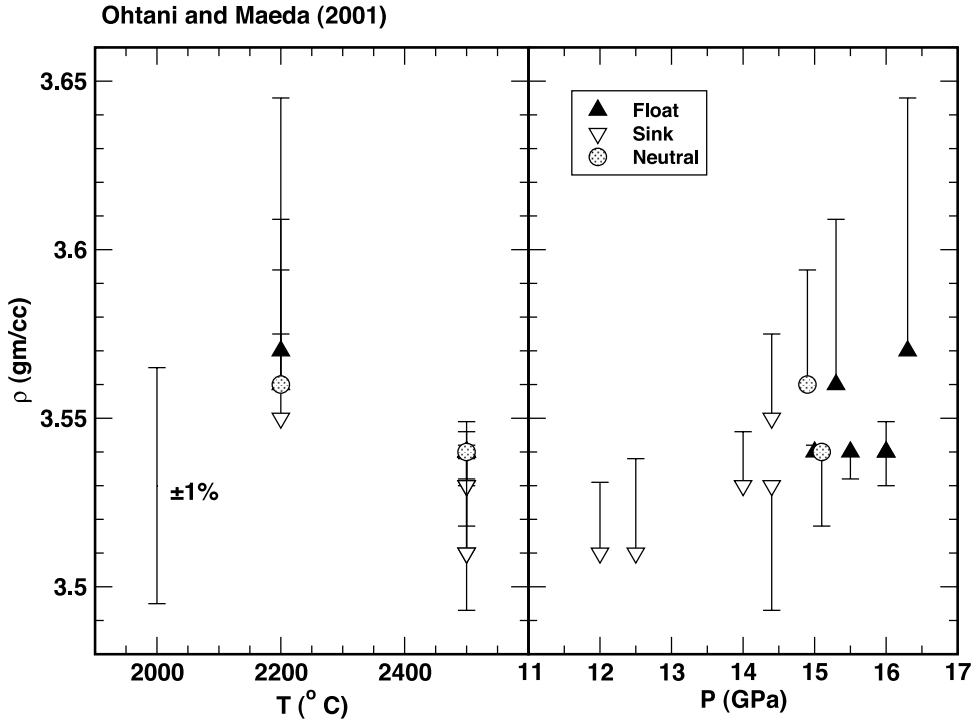


Fig. 5. Analysis of sink-float experimental data of Ohtani and Maeda (2001) on MORB and picritic melts using diamond as a density marker. Symbol usage, axes content and labels follows figure 1. An uncertainty bracket of  $\pm 1\%$  is provided for reference.

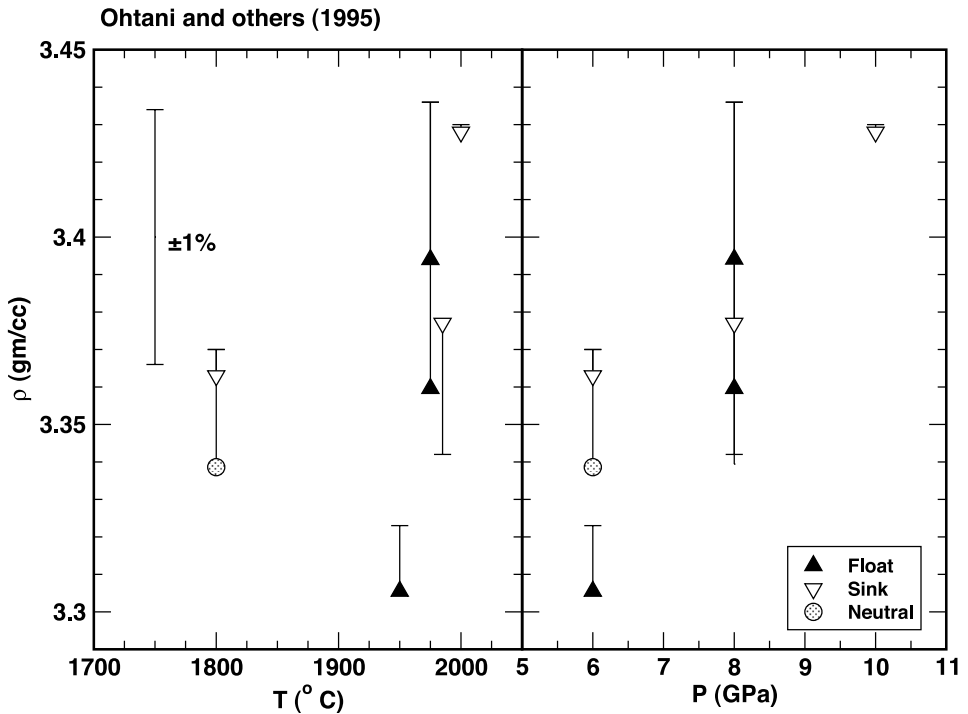


Fig. 6. Analysis of sink-float experimental data of Ohtani and others (1995) on FeO-rich peridotite composition liquids (model compositions for the Martian mantle) using olivine as a density marker. Symbol usage, axes content and labels follows figure 1. An uncertainty bracket of  $\pm 1\%$  is provided for reference.

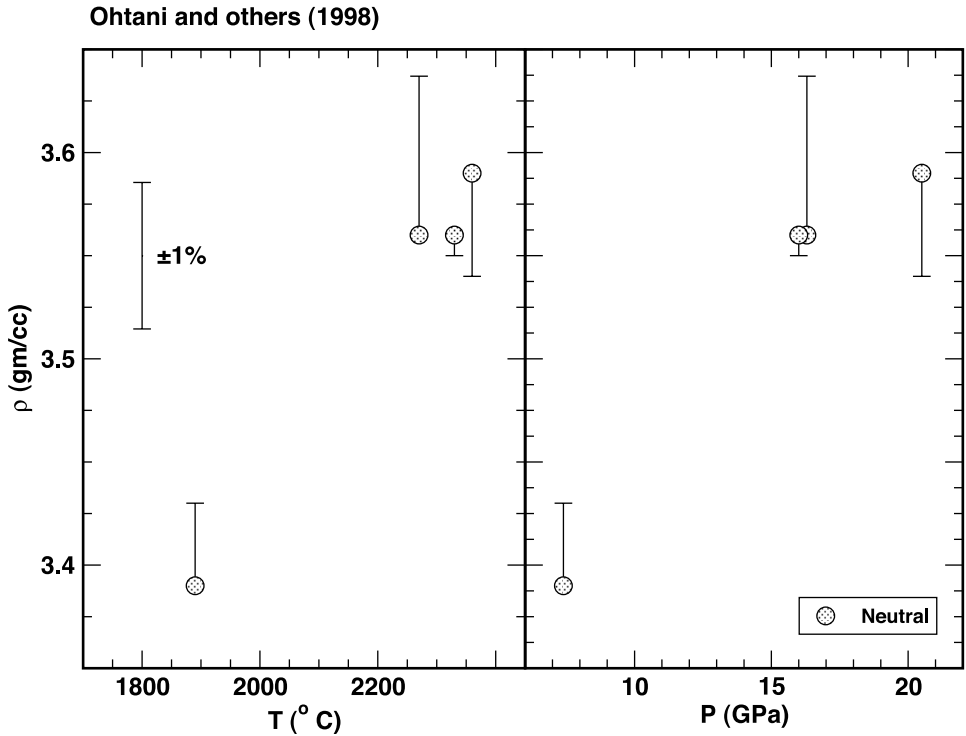


Fig. 7. Analysis of sink-float experimental data of Ohtani and others (1998) on FeO-rich peridotite composition liquids (model compositions for the Martian mantle) using olivine and diamond as density markers. Symbol usage, axes content and labels follow figure 1. An uncertainty bracket of  $\pm 1\%$  is provided for reference.

mixing model of Part II does not extrapolate to melts of these compositions. Densities inferred from the fusion curve of pyrope are also systematically under predicted. In the absence of data on CN-speciation in  $\text{Mg}_3\text{Al}_2\text{Si}_3\text{O}_{12}$  liquid, these data were modeled in Part III and treated here by ignoring configurational contributions to the volume. In light of the molecular dynamics results on  $\text{CaAl}_2\text{Si}_2\text{O}_8$  and  $\text{CaMgSi}_2\text{O}_6$  liquids, this assumption is clearly in error, but the effects are difficult to assess quantitatively. The current analysis suggests that configurational collapse may increase the melt density by  $\sim 4$  percent at the average pressure of the pyrope fusion curve experiments ( $\sim 7$  GPa).

Density data on melts with high Ti-contents are modeled very well as demonstrated by the recovery of the data of Circone and Agee (1996) and the titanite fusion curve.

High-pressure model parameters for  $\text{K}_2\text{O}$  are constrained from only two data sets in the calibration: liquid densities inferred from the fusion curve of sanidine (data span the range 2 - 4 GPa, see Part III) and the composition of Miller and others (1991), which contains a scant 0.25 weight percent  $\text{K}_2\text{O}$ . These constraints are inadequate for accurately defining mixing parameters for  $\text{K}_2\text{O}$  over a broad compositional range, and the resulting model should be used with caution (or better yet not at all) to calculate the densities of highly potassic mafic liquids at pressure.

#### RECOMMENDED MODEL USAGE AND LIMITATIONS OF THE CALIBRATION

The optimized EOS high-pressure mixing parameters reported in table 2 are weighted heavily towards ultramafic and mafic composition silicate liquids. Over the

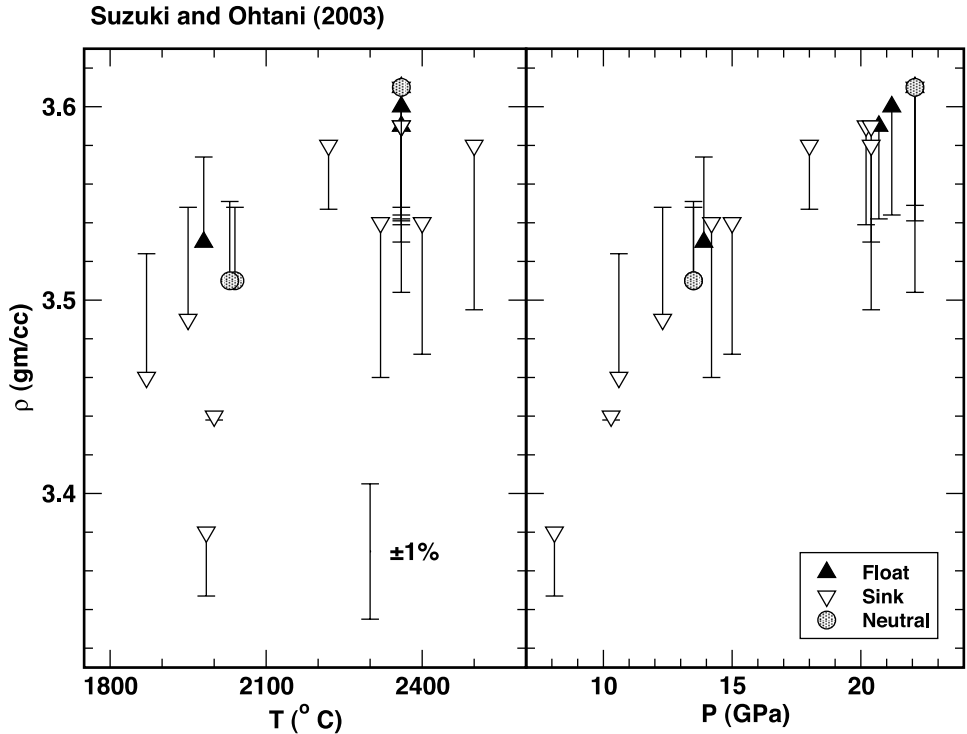


Fig. 8. Analysis of sink-float experimental data of Suzuki and Ohtani (2003) on peridotite composition liquids using olivine and diamond as density markers. Symbol usage, axes content and labels follow figure 1. An uncertainty bracket of  $\pm 1\%$  is provided for reference.

temperature range of  $\sim 1000$  to  $2500^{\circ}\text{C}$  and pressure range of 0 to 40 GPa, these parameters can be utilized in conjunction with those from Part II to calculate the densities of basaltic to komatiitic liquids with an expected error of about 2 percent. The paucity of experimental data available on the densities of multicomponent silicate liquids at elevated pressure, especially outside of the compositional range of liquids used in sink-float experiments, makes calibration of more sophisticated, and presumably nonlinear, mixing models for high-pressure EOS parameters problematic. Even more limiting is the lack of information on the effects of changing melt structure on density. For practical reasons, calibration of the model parameters reported here rely upon various CN-speciation thermodynamic models *applied separately* to compositionally simple melts, high-Ti lunar liquids, other basaltic liquids, and ultramafic liquids. This procedure raises the question of what should be done for intermediate composition liquids? The best suggestion to be made at this stage is to interpolate between the various CN-speciation models developed in Part III. A more sophisticated approach will require more data: an expanded data set of sink-float experiments, more complex liquids studied by shock-compression, direct measurement of the sound speed in silicate melts at pressure, and an extensive campaign of molecular dynamics simulation.

Even within the restricted composition space of basaltic to komatiitic/peridotitic liquids, a significant limitation of the model calibration developed in this paper is the restriction to systems that do not contain appreciable amounts of oxidized iron and that do not contain dissolved volatiles ( $\text{H}_2\text{O}$  or  $\text{CO}_2$ ). As noted above, the relative

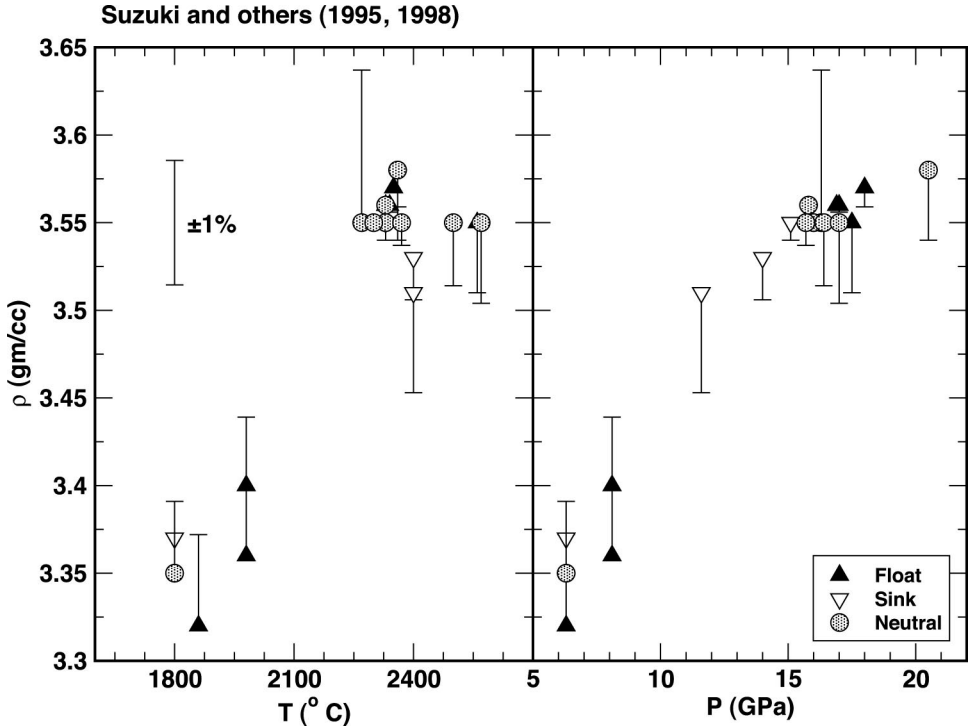


Fig. 9. Analysis of sink-float experimental data of Suzuki and others (1995, 1998) on FeO-rich peridotite composition liquids (model compositions for the Martian mantle) using olivine and diamond as density markers. Symbol usage, axes content and labels follow figure 1. An uncertainty bracket of  $\pm 1\%$  is provided for reference.

magnitudes of the molar volumes of FeO, FeO<sub>1.3</sub> and FeO<sub>1.5</sub> (Part II) lead to the expectation that at constant redox potential, the melt ferric/total-iron ratio should decrease with increasing pressure. Therefore, under expected oxidation state and pressure conditions relevant to the Earth's mantle it is unlikely that the concentration of Fe<sub>2</sub>O<sub>3</sub> in partial melts will be significant enough to affect first order estimates of melt densities. Unfortunately, the absence of high-pressure mixing parameters for oxidized Fe-species prevents the estimation of the partial molar volumes of the FeO<sub>1.3</sub> and FeO<sub>1.5</sub> components in the liquid at pressure and this in turn prevents the calculation of the chemical potentials of these components. Addition of volatiles to the model EOS awaits sink-float density measurements in water and carbon dioxide bearing melts of *similar composition* to the anhydrous experiments dealt with here. Available data on water rich feldspar-like liquids, when combined with measurements on anhydrous mafic melts, prevent the assessment of the effects of water independently of the variation in major element composition.

Despite the considerable number and the restrictive character of the limitations on the model, the EOS mixing parameters reported in table 2 should facilitate the calculation of the volumetric and related thermodynamic properties of anhydrous, reduced, ultramafic to MORB-like composition liquids to pressures in the Earth corresponding to the base of the mantle transition zone. There is at present no viable alternative thermodynamically consistent interpolative scheme for estimating the densities of potential mantle partial melts. And, without a model of this kind, however

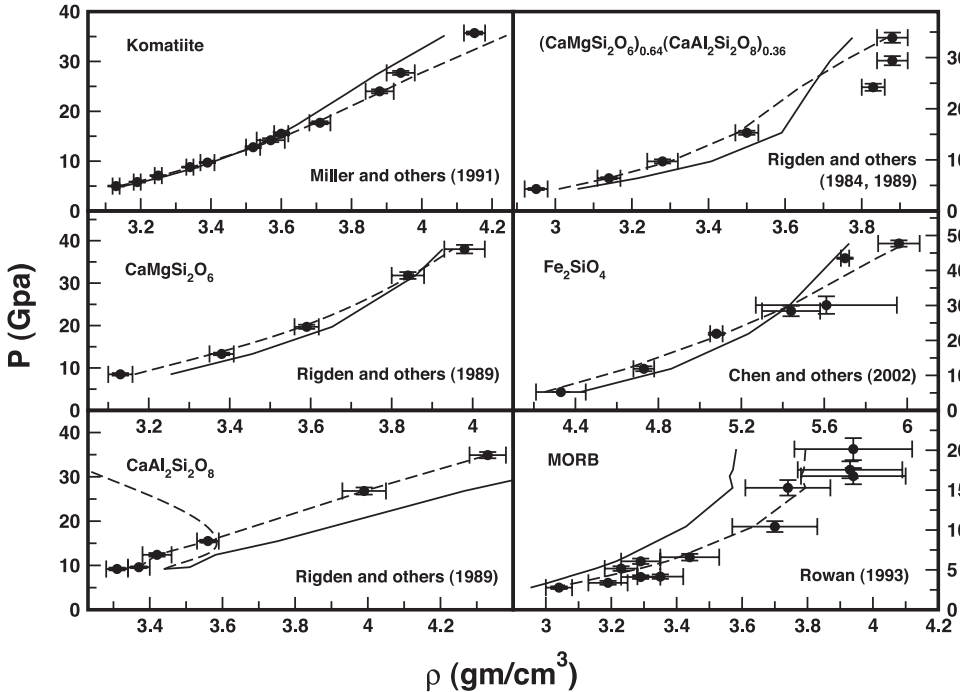


Fig. 10. Analysis of shock compression experiments considered as model calibrants for high-pressure EOS mixing parameters. Data points indicate measurements from represented studies with error bars as reported. Dashed lines are optimal Hugoniot fits from Part III. Solid lines are Hugoniot curves derived from the mixing parameterization developed in this paper. Pressure is plotted on the ordinate in units of GPa and density is plotted on the abscissa in units of grams/cm<sup>3</sup>. The two dashed curves plotted for CaAl<sub>2</sub>Si<sub>2</sub>O<sub>8</sub> composition liquid represent alternative model Hugoniots, neither of which are internally consistent with both the density and the internal energy of the shock compression experiments (see Part III).

preliminary, there is no means of evaluating the Gibbs free energy of the liquid phase, which is necessary for the construction of thermodynamic models of mantle melting.

Why is a thermodynamic model of mantle melting needed? In the context of lower upper-mantle and transition zone melting, a critical issue that must be appreciated is the buoyancy of *equilibrium partial melts* relative to residual solid phases. Is the equilibrium partial melt more or less dense than *every solid* phase in the residual assemblage, and if not is net buoyancy of the melt positive or negative? At what fraction of partial melting does the liquid become more or less dense than coexisting solids? And, do the effects of water enhance – as might be expected intuitively by analogy with low-pressure studies – or decrease (as suggested by Bercovici and Karato, 2003) melt buoyancy at transition zone pressures? Results from sink-float experiments alone do not resolve these questions, and at present answers are purely speculative. Shoring up the speculation with more quantitative arguments requires a thermodynamic model of mantle phase relations in the 3 to 40 GPa range. The equation of state calibration developed here is the first step along the path towards that goal. The next step will be to combine this work with experimental data on solid liquid phase equilibria to construct a preliminary thermodynamic model for mantle melting to pressures of 40 GPa. Research along these lines is ongoing and results will be the subject of a future contribution.

## ACKNOWLEDGMENTS

Material support for this investigation was generously provided by the National Science Foundation (OCE-9977416 and EAR-9980518) and The University of Chicago.

## APPENDIX

The proposed liquid EOS,

$$V = \frac{V_{0,T} + (V_{1,T} + V_{0,T}a)(P - P_r) + \left(\frac{V_2}{2} + V_{1,T}a + V_{0,T}b\right)(P - P_r)^2}{1 + a(P - P_r) + b(P - P_r)^2} \quad (\text{A-1})$$

will develop pole-singularities if the parameters  $a$  and  $b$  assume values that yield positive real roots ( $P_{crit}$ ) of the quadratic polynomial

$$1 + a(P - P_r) + b(P - P_r)^2 = 0 \quad (\text{A-2})$$

The roots of equation (A-2) are given by

$$P_{crit} = P_r - \frac{a}{2b} \pm \frac{\sqrt{a^2 - 4b}}{2b} \quad (\text{A-3})$$

In order to avoid the singularities that lead to non-physical solutions of the EOS, values of  $a$  and  $b$  must be bounded so that real solutions of equation (A-3) are negative. This effectively means that all solutions of equation (A-3) for  $P_{crit}$  are permissible, *both real and complex*, except those along the positive branch of the real axis. Writing  $P_{crit}$  explicitly as a complex quantity,

$$P_{crit} = \text{Re}(P_{crit}) + i \text{Im}(P_{crit}) \quad (\text{A-4})$$

equation (A-3) becomes

$$\text{Re}(P_{crit}) = \begin{cases} P_r - \frac{a}{2b} \pm \frac{\sqrt{a^2 - 4b}}{2b} & a^2 - 4b \geq 0 \\ P_r - \frac{a}{2b} & a^2 - 4b < 0 \end{cases} \quad (\text{A-5a})$$

and

$$\text{Im}(P_{crit}) = \begin{cases} 0 & a^2 - 4b \geq 0 \\ \sqrt{4b - a^2}/2b & a^2 - 4b < 0 \end{cases} \quad (\text{A-5b})$$

The pair of numbers  $[\text{Re}(P_{crit}), \text{Im}(P_{crit})]$  may be considered as Cartesian coordinates defining  $P_{crit}$  in the complex plane. It is convenient to map this set of Cartesian coordinates to Polar coordinates,  $[r(a,b), \theta(a,b)]$ , where

$$r(a,b) = \sqrt{[\text{Re}(P_{crit})]^2 + [\text{Im}(P_{crit})]^2} \quad (\text{A-6})$$

and

$$\tan \theta(a,b) = \frac{\text{Im}(P_{crit})}{\text{Re}(P_{crit})}, \quad (\text{A-7})$$

and where  $\theta(a,b)$  is an angle measured relative to the positive branch of the real axis,  $0 \leq \theta \leq 2\pi$ . The operative constraint that  $P_{crit} \leq 0$  for real solutions to equation (A-3) then reduces to a simple constraint on  $\theta(a,b)$ , namely  $0 < \theta(a,b) < 2\pi$ . In this form the constraint can be imposed as a simple non-linear bound on permissible  $(a,b)$ -pairs that are suitable for physically realistic solutions of the EOS. Recall that a bound constraint on  $(a,b)$ -pairs translates into a constraint on permissible values of model mixing parameters ( $\bar{v}_{2,i}$ ,  $\bar{v}_{3,i}$ , and  $\bar{v}_{4,i}$ ) via equations (2), (3), (14), (15) and (16).

## REFERENCES

- Agee, C. B., 1992a, Isothermal compression of molten  $\text{Fe}_2\text{SiO}_4$ : *Geophysical Research Letters*, v. 19, p. 1169-1172.
- 1992b, Thermal expansion of molten  $\text{Fe}_2\text{SiO}_4$  at high pressure: *Geophysical Research Letters*, v. 19, p. 1173-1176.
- Agee, C. B., and Walker, D., 1988, Static compression and olivine flotation in ultrabasic silicate liquid: *Journal of Geophysical Research*, v. 93, p. 3437-3449.
- 1993, Olivine flotation in mantle melt: *Earth and Planetary Science Letters*, v. 114, p. 315-324.
- Angell, C. A., Cheeseman, P. A., and Kadiyala, R. R., 1987, Diffusivity and thermodynamic properties of diopside and jadeite melts by computer simulation studies: *Chemical Geology*, v. 62, p. 83-92.
- Belonoshko, A. B., and Dubrovinsky, L. S., 1996, Molecular and lattice dynamics study of the  $\text{MgO-SiO}_2$  system using a transferable interatomic potential: *Geochimica et Cosmochimica Acta*, v. 60, p. 1645-1656.
- Bercovici, D., and Karato, S. I., 2003, Whole-mantle convection and the transition-zone water filter: *Nature*, v. 425, p. 39-44.
- Bryce, J. G., Spera, F. J., and Stein, D. J., 1999, Pressure dependence of self-diffusion in the  $\text{NaAlO}_2\text{-SiO}_2$  system: Compositional effects and mechanisms: *American Mineralogist*, v. 84, p. 345-356.
- Carmichael, I. S. E., and Ghiorsio, M. S., 1986, Oxidation-reduction relations in basic magma: a case for homogeneous equilibria: *Earth and Planetary Science Letters*, v. 78, p. 200-210.
- Chen, G. Q., Ahrens, T. J., and Stolper, E. M., 2002, Shock-wave equation of state of molten and solid fayalite: *Physics of the Earth and Planetary Interiors*, v. 134, p. 35-52.
- Circone, S., and Agee, C. B., 1996, Compressibility of molten high-Ti mare glass: Evidence for crystal-liquid density inversions in the lunar mantle: *Geochimica et Cosmochimica Acta*, v. 60, p. 2709-2720.
- Diefenbacher, J., McMillan, P. F., and Wolf, G. H., 1998, Molecular dynamics simulations of  $\text{Na}_2\text{Si}_4\text{O}_9$  liquid at high pressure: *Journal of Physical Chemistry B*, v. 102, p. 3003-3008.
- Ghiorsio, M. S., 2004a, An Equation of State for Silicate Melts. I. Formulation of a General Model: *American Journal of Science*, v. 304, p. 637-678.
- 2004b, An Equation of State for Silicate Melts. III. Analysis of stoichiometric liquids at elevated pressure: shock compression data, molecular dynamics simulations and mineral fusion curves: *American Journal of Science*, v. 304, p. 752-810.
- Ghiorsio, M. S., and Kress, V. C., 2004, An Equation of State for Silicate Melts. II. Calibration of volumetric properties at  $10^3$  Pa: *American Journal of Science*, v. 304, p. 679-751.
- Ghiorsio, M. S., and Sack, R. O., 1995, Chemical Mass Transfer in Magmatic Processes IV. A revised and internally consistent thermodynamic model for the interpolation and extrapolation of liquid-solid equilibria in magmatic systems at elevated temperatures and pressures: *Contributions to Mineralogy and Petrology*, v. 119, p. 197-212.
- Ghiorsio, M. S., Hirschmann, M. M., Reiners, P. W., and Kress, V. C., III, 2002, The pMELTS: A revision of MELTS for improved calculation of phase relations and major element partitioning related to partial melting of the mantle to 3 GPa: *Geochemistry, Geophysics, Geosystems*, v. 3(5), 10.1029/2001GC000217.
- Huebner, J. S., 1971, Buffering technique for hydrostatic systems at elevated pressures, in *Research Techniques for High Pressure and High Temperature*, edited by G. C. Ulmer: New York, Springer-Verlag, p. 123-177.
- Knoche, R., and Luth, R. W., 1996, Density measurements on melts at high pressure using the sink/float method: Limitations and possibilities: *Chemical Geology*, v. 128, p. 229-243.
- Kress, V. C., and Carmichael, I. S. E., 1991, The compressibility of silicate liquids containing  $\text{Fe}_2\text{O}_3$  and the effect of composition, temperature, oxygen fugacity and pressure on their redox states: *Contributions to Mineralogy and Petrology*, v. 108, p. 82-92.
- Kubicki, J. D., and Lasaga, A. C., 1991, Molecular dynamics simulations of pressure and temperature effects on  $\text{MgSiO}_3$  and  $\text{Mg}_2\text{SiO}_4$  melts and glasses: *Physics and Chemistry of Minerals*, v. 17, p. 661-673.
- Matsui, M., 1996, Molecular dynamics simulation of structures, bulk moduli, and volume thermal expansivities of silicate liquids in the system  $\text{CaO-MgO-Al}_2\text{O}_3\text{-SiO}_2$ : *Geophysical Research Letters*, v. 23, p. 395-398.
- Miller, G. H., Stolper, E. M., and Ahrens, T. J., 1991, The equation of state of a molten komatiite I. Shock wave compression to 36 GPa: *Journal of Geophysical Research*, v. 96, p. 11831-11848.
- Morgan, N. A., and Spera, F. J., 2001a, Glass transition, structural relaxation, and theories of viscosity: A molecular dynamics study of amorphous  $\text{CaAl}_2\text{Si}_2\text{O}_8$ : *Geochimica et Cosmochimica Acta*, v. 65, p. 4019-4041.
- 2001b, A molecular dynamics study of the glass transition in  $\text{CaAl}_2\text{Si}_2\text{O}_8$ : Thermodynamics and tracer diffusion: *American Mineralogist*, v. 86, p. 915-926.
- Nevins, D., and Spera, F. J., 1998, Molecular dynamics simulations of molten  $\text{CaAl}_2\text{Si}_2\text{O}_8$ : Dependence of structure and properties at pressure: *American Mineralogist*, v. 83, p. 1220-1230.
- Ohtani, E., and Maeda, M., 2001, Density of basaltic melt at high pressure and stability of melt at the base of the lower mantle: *Earth and Planetary Science Letters*, v. 193, p. 69-75.
- Ohtani, E., Nagata, Y., Suzuki, A., and Kato, T., 1995, Melting relations of peridotite and the density crossover in planetary mantles: *Chemical Geology*, v. 120, p. 207-221.
- Ohtani, E., Suzuki, A., and Kato, T., 1998, Flotation of olivine and diamond in mantle melt at high pressure: Implications for fractionation in the deep mantle and ultradeep origin of diamond: *American Geophysical Union Geophysical Monograph*, v. 101, p. 227-239.
- Rigden, S. M., Ahrens, T. J., and Stolper, E. M., 1984, Densities of liquid silicates at high pressures: *Science*, v. 226, p. 1071-1074.

- 1988, Shock compression of molten silicate: results for a model basaltic composition: *Journal of Geophysical Research*, v. 93, p. 367-382.
- 1989, High-pressure equation of state of molten anorthite and diopside: *Journal of Geophysical Research*, v. 94, p. 9508-9522.
- Rowan, L. R., ms, 1993, I. Equation of state of molten mid-ocean ridge basalt. II. Structure of Kilauea volcano: Ph.D. dissertation, California Institute of Technology, U.M.I. #9316860.
- Smith, J. R., and Agee, C. B., 1997, Compressibility of molten "green glass" and crystal-liquid density crossovers in low-Ti lunar magma: *Geochimica et Cosmochimica Acta*, v. 61, p. 2139-2145.
- Suzuki, A., and Ohtani, E., 2003, Density of peridotite melts at pressure: *Physics and Chemistry of Minerals*, v. 30, p. 449-456.
- Suzuki, A., Ohtani, E., and Kato T., 1995, Flotation of diamond in mantle melt at high pressure: *Science*, v. 269, p. 216-218.
- 1998, Density and thermal expansion of a peridotite melt at high pressure: *Physics of the Earth and Planetary Interiors*, v. 107, p. 53-61.
- Wasserman, E. A., Yuen, D. A., Rustad, J. R., 1993, Compositional effects on the transport and thermodynamic properties of MgO-SiO<sub>2</sub> mixtures using molecular dynamics: *Physics of the Earth and Planetary Interiors*, v. 77, p. 189-203.
- Zhou, Y., and Miller, G. H., 1997, Constraints from molecular dynamics on the liquidus and solidus of the lower mantle: *Geochimica et Cosmochimica Acta*, v. 61, p. 2957-2976.